Energy management of lossy multi-port to fuel cell-based systems

Victor Manuel Ramirez Rivera

UNIVERSITE PARIS-SUD

ÉCOLE DOCTORALE
Sciences et Technologie de l'Information, des Télécommunications et des Systèmes
Laboratoire des signaux et systèmes

DISCIPLINE : PHYSIQUE

THÈSE DE DOCTORAT

Soutenance prévue le 16/05/2014

par

Victor Manuel RAMIREZ RIVERA

Energy Management of Lossy Multi-Port to Fuel Cell-Based Systems
Gestion de l'énergie d'un Système Multi-Port à Pertes Intégrant une Pile à Combustible

Composition du jury :

Directeur de thèse :	**Romeo ORTEGA**	**Directeur de Recherche CNRS (L2S)**
Co-encadrant de thése:	**Olivier BETHOUX**	**Maître de Conférences HDR (LGEP)**
Rapporteurs :	Malek GHANES	Maître de Conférences HDR (ENSEA)
	Mohamed BECHERIF	Maître de Conférences HDR (FCLAB)
Examinateurs :	Dorothee NORMAND-CYROT	**Directeur de Recherche CNRS (L2S)**
	Robert GRIÑO	Directeur de Recherche (UPC)
Membres invités :	Elena PANTELEY	Chargé **de Recherche CNRS (L2S)**

Contents

Notation

List of Symbols

t is time
N is number of ports
R is linear resistive element
i_j is current vector of system
v_j is voltage vector of system
H_j is stored energy
P_j is supplied power
d_j is dissipation power
Σ is port of system
α is profile reference
L_i is inductor element
C_i is capacitor element
F_j is current vector
V is Lyapunov function
E_{th} is Nerts tension
V_{ohm} is activation voltage
V_{act} is ohmic voltage
V_{con} is concentration voltage
θ is oxygen pressure
T_{atm} is atmospheric temperature
p_{atm} is atmospheric pressure
ρ_{h_2} is hydrogen pressure
p_{sat} is saturation pressure vapor
T_{st} is fuel cell stack temperature
A_{fc} is cell active area
I_{max} is maxim current density

Abbreviations

PEM	Polymer Exchange Membrane
I&I	Immersion and Invariance
PI	Proportionnel–Intégral
RED	Routeur d'Énergie Dynamique
DS–RED	Duindam Stramigioli Routeur d'Énergie Dynamique
PAC	Pile à Combustible
PEMPAC	Polymer Exchange Membrane Pile à Combustible
ECG	Estimateur Convergent Globalement
LTI	Linear Time Invariant
SCs	Super–Condensateurs
IGBT	Insulated Gate Bipolar Transistor
FC	Fuel Cell
PEMFC	Polymer Exchange Membrane Fuel Cell
DER	Dynamic Energy Router
DS–DER	Duindam Stramigioli Dynamic Energy Router
PWM	Pulse Wide Modulated
DC	Direct Current
PI	Proportional–Integral
GCEOP	Globally Convergent Estimator of Oxygen Pressure

Introduction

The objectives of this thesis work are: *i*) prove a new strategy to transfer energy in a dynamic interconnection system composed of electrical circuit components: resistors, capacitors, and inductors (passive elements), and switching semiconductors; power transistors as Insulated Gate Bipolar Transistor (IGBT), Metal-oxide-semiconductor Field-effect Transistor (MOSFET), Thyristors and Diodes, and *ii*) design of a globally convergent estimator of pressure for a fuel cell type polymer exchange membrane by using the principles of "Immersion and Invariance" recently reported in control theory.

Motivation

The attractive, worrying, and urgent topics of actual research are energy generation problems. In this direction, some approaches have been proposed to offer solutions for particular cases, for different study areas. Inside of the mathematic field, the control domain is investigating the development of a new fundamental theory. This new theory is our motivation to implement successfully this advance in renewable energy sources. Specifically sources like the fuel cell and its corresponding interconnection system. Considering that the nonlinear behavior of both systems should be analyzed with nonlinear methods, by using some mathematical tools and simulations to converge a favorable result, for a future implementation in the transport.

Problem Statement

The dependency on oil, the pollution products of fuel combustion, the excessive consumption of energy in industry even at home, the global warming between other affectations are the consequences for our planet of nonrenewable energy consumption. These problems have been obligated to the scientific community to provide specific solutions in these kind of topics, as was reported in [1], [2]. In the transport domain the science is searching for an alternative to non renewable energies or new advances in some existing renewable energies. The fuel cell is one alternative, it is a renewable energy proposed as a good solution for trying to revert the problematic energy production, however, it is still in

research. The nonlinear control design of the fuel cell and its auxiliaries, the complex nonlinear modeling, and the parameter estimations, are some topics to investigate in this system, furthermore, these subjects should be solved together with some interconnection problems for these microgrids.

State of the Art

Transport energy evolution

Transport systems are complex nonlinear dynamic models, which uses energy such as thermic, electrical, chemical, etc to move persons or objects from one location to another. Water, air, and land mobile vehicles are the typical examples of general transports, however, land vehicles (motorcycles, cars, buses, trains, etc) are more employed than water and air vehicles to interact in many human tasks.

An historical example of the first land vehicle inventions date back to the year 1769 with the of Cugnot Steam Trolley (Fig. 3) designed by Jonathan Holguinisburg, which was invented to transport goods using a steam engine to power it.

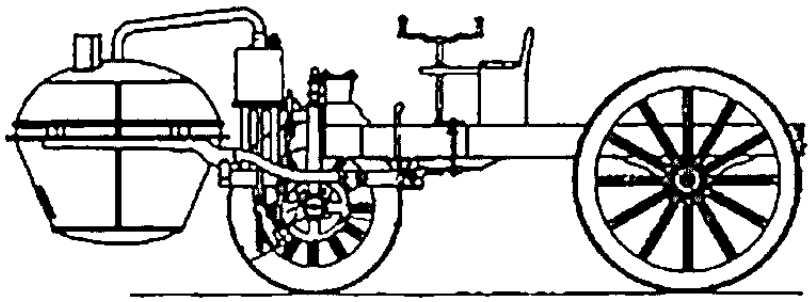

Figure 1: Cugnot Steam Trolley 1769

After invention of these early transports, the evolution in the following centuries in terms of energy consumption when using petroleum–based fuels with the actual consequences like air pollution, shortage of energy, and global warming, affect the environment of our planet with several nonreversible ecological impacts.

Today, those energy problems imply redesigning and improving new energy supplies in transport [3]. The electric, hybrid, solar, and fuel cell vehicles have been aimed to solve these problems. We are especially interested in the fuel cell vehicle; an example design of this kind of vehicles is shown in Fig. 4. This new generation of mobile transport usually present interconnection system problems [33] owing to the nonlinearities immerse in electric components, power converters, charges, and loads.

To solve these problems, energy management strategies are proposed for general cases of the interconnections with an emphasis on fuel cell–based systems. There are two

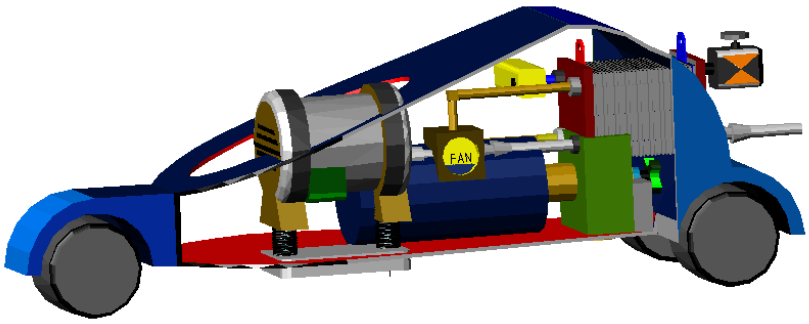

Figure 2: Fuel Cell Vehicle Design

strategies that are shown in this work; the first employed a Duindam–Stramigioli Dynamic Energy Router (DS–DER) reported in [32], [5], and [6]. This strategy consists of generating the current or voltage references—see, eg, [22], [23], [30], and [31], with the objective of regulating the change and rate of current flow in this microgrid. Implementing some controllers like Proportional–Integral (PI), Feedback Linearization (FB), and Input-Output Linearization (IOL). Following the principles of Control-by-Interconnection [34], the DS–DER strategy to dynamically control the energy flow between *lossless* multiports, with its corresponding power electronics implementation in a standard circuit topologies is tested.

The second strategy is redesigning the DER. Knowing that the dissipation present in each element of the interconnections subtracts the energy of the system enunciated by energy conservation law, which is a feature of passive systems, reported in [7]. We can compensate for these losses by adding an energy supply.

Finally, it is necessary to board the integral problem of both; the energy management strategies, and the fuel cell system, seen in [10], [11], and [12], to ensure the overall operation. Also, we need further research about the nonlinear dynamical model of this energy source and their auxiliaries to incorporate a multi-variable adaptive control design [9], [8].

Polymer exchange membrane-fuel cell

The principle of the fuel cell was discovered in 1838 by the German chemist Christian Friederich Schönbein, who published his work in a philosophical magazine in 1839. At the same time, the work of Sir William Grove introduces the concept of the hydrogen fuel cell. He generated energy through the immersion of two platinum electrodes in a solution of sulfuric acid with the other ends separately sealed in containers of oxygen and hydrogen, finding a constant current to flow between the electrodes. After the discovery of this physical principle, the improvement of fuel cells evolved to the actual present as the work cited in [4] shows.

Actually, many kinds of fuel cells exist with different applications. Our case study is focused polymer exchange membrane fuel cells (PEMFC), which are employed in transport domains due to small dimensions and high efficiency. These electromechanical-chemical devices generate electricity through a chemical reaction between a group of gases (eg, hydrogen, oxygen) and a catalyst. The basis of the physical phenomenon principle of PEMFC exposed in [44] and [45] give us fundamental physical laws to formulate the nonlinear mathematical model in [43]. To carry out the analysis with the PEMFC mathematical model, it is usually divided into two subsystems; (i) the compressor, which is composed of motion mechanical parts; and (ii) the fuel cell stack, which is using integrates static mechanical elements (Fig. 5), both are modeled by a group of differential equations as a new reduction model developed in [42], however, an alternative for modeling the electrical output of the fuel cell is parameterizing the voltage-current curve with some mathematical relationships.

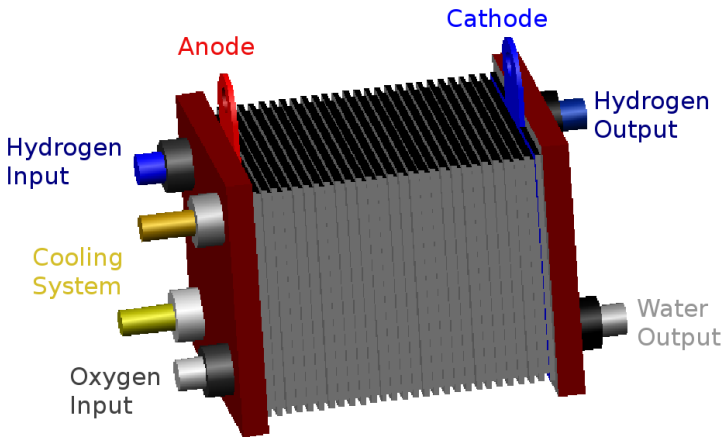

Figure 3: Fuel Cell Stack

The electrical output behavior of PEMFC is commonly represented by a voltage-current curve. This mathematical relationship depends on physical variables and parameters of mechanical-electrical-chemical design that evolves with time. For the analysis of FCs with their auxiliaries (Fig. 6), it is necessary to know certain physical variables like: humidity, temperature, pressure, voltage, and current. This set of variables (usually measured by electrical-electronic sensors) permits on data evaluate using a computer to some specific purposes such as whether the FC is working in the correct physical limits, to prevent damage and aging of the system, to analyze and validate the dynamic mathematical model *vs* the real model, and to design the nonlinear control of the plant with

feedback loop measurements. However, FC variables are not convenient to measure. The pressure present in the pipeline of PEMFC gases (hydrogen and oxygen) is one, because this measurement device is expensive, it needs frequent maintenance, useful life is short, the distribution and adaptation of small plants are limited, and the display of the pressure value is not exact. To solve these problems, a globally convergent estimator (GCE) of pressure design for this application is proposed by using the principles of the Immersion and Invariance theory recently reported in a literature review in [37], [38].

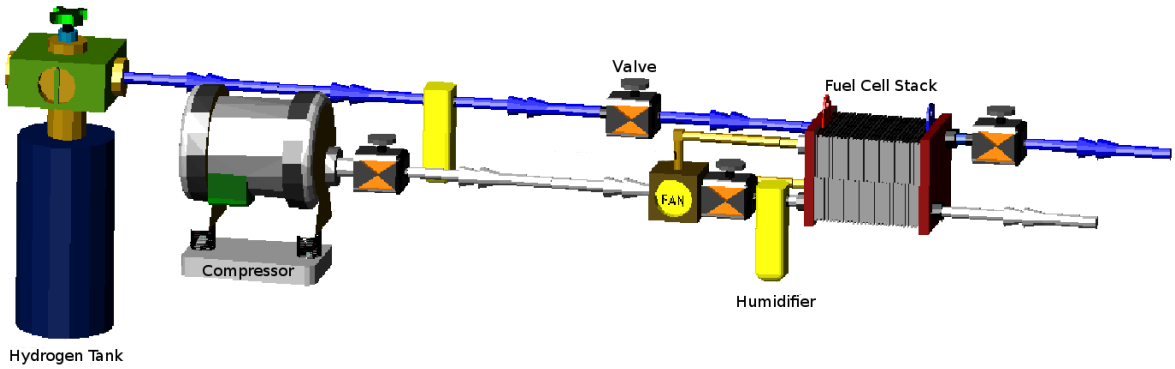

Figure 4: PEM Fuel Cell and their Auxiliaries

In the case of hydrogen gas pressure, it is not included in our problem because it is supplied by tanks. This equates to a constant value of pressure for this specific gas. The oxygen gas pressure is taken from the environment through an air compressor. This electrical machine is responsible for the increase or decrease in the oxygen pressure in the PEMFC pipes. It is included when we board the dynamical model analysis. In the estimation case of variable pressure, we have reconstructed it from measurements [35], [36]. Ensuring stability, by calling upon Lyapunov's second theorem, if our FC behavior function is strictly monotonically increased [39].

Outline of the thesis

A new method of energy transfer through a strategy called "Duindam Stramigioli Dynamic Energy Router" (DS–DER) is explained in the first Chapter, considering that a nonlinear system of interconnections composed of energy sources and loads present dynamic transference of energy between them. This DS–DER can regulate the flow of current and the tension of energy blocks called "multiports", if and only if, the interconnection system is lossless.

After the first assumption, in the second Chapter, we have reconsidered the same problem, but now with evidence that we have losses, therefore, they are present in the nonlinear interconnection system. To analyze this new problem, the proposal is changed

to implement a New Dynamic Energy Router (New DER) with the same objective of a DS–DER. The energy transfer results are presented over a long period of time with evident differences between both methods.

The third Chapter addresses the problem of pressure estimation in a proton exchange membrane fuel cell (PEMFC) system. The design of a globally convergent estimator is developed taking the PEMFC behavior function of voltage–current, where we have; measurable and nonmeasurable variables. Nonmeasurable variables exhibit some difficulties to be direct by measured in a PEMFC. To solve this problem we propose specifically reconstructing the oxygen pressure variable of PEMFC with measurable variables by means of an estimator that uses principle of Immersion and Invariance (I&I) control theory.

Finally, the concluding remarks about the work in this discuss, the advantages, disadvantages, and the future work.

Chapter 1

Duindam–Stramigioli Dynamic Energy Router

1.1 Introduction

This chapter proposes a topology of electrical energy transfer systems commonly presented in electrical vehicles as a typical example, this operation principle regulates energy between subsystems can be generating, storing, or consuming. However, efficient transfer of electrical energy is a current problem immersed in a group of multidomain systems consisting of a generation unit, batteries, supercapacitors, and electric motors or generators. Depending on the operation regime, energy must be transferred between the various units, which are called multiports, according to some energy–management policies. In order to ensure energy exchange, the interconnection of the storage and load devices is performed by using power converters. These subsystems are electronic devices that work as electric switched circuits that are able to regulate port voltages or current flows to reference values.

To achieve energy transfer between multiports, it is common practice to assume that the system operates in steady state and then translates the power demand (flow sense and magnitude) of the multiports into current or voltage references. These references are then tracked with control loops, usually proportional plus integral (PI). Since the various multiports have different time responses, it is often necessary to discriminate between quickly and slowly changing power–demand profiles. For instance, due to physical constraints, it is not desirable to quickly demand changing power profiles to a generation unit. Hence, the peak demands of the load are usually supplied by a bank of supercapacitors, whose time response is fast. To achieve this objective, a steady–state viewpoint is again adopted, and the current or voltage references to the multiports are passed through lowpass or highpass filters.

The steady–state approach currently adopted in practice can only approximately

achieve the desired objectives of energy transfer and slow–versus–fast discrimination of the power demand. In particular, during the transients or when a fast dynamic response is required, the delivery of demanded power in response to current or voltage references and the time response action of the filters might be far from satisfactory.

In this chapter, an energy router that dynamically controls energy flow is presented. The router operational principle presented in [13], [14] is within the context of walking robots. A brief review of this device, which we call the Duindam–Stramigioli dynamic energy router (DS–DER), is given below from the perspective of electrical networks. The DS–DER embodies a nonlinear transformation that instantaneously transfers energy among multiports. The flow direction and rate of change of the energy transfer are regulated by means of a single scalar parameter. The goal of this work is to show that the DS–DER can be implemented by using standard power electronic converter topologies; see [15], [18], [19]. Moreover, it is shown in [20], [21] that nonlinear controllers can be used to determine the switching policy of the power converter. Therefore, the DS–DER can provide the basis for a physically viable device for high–performance energy–management applications. A DS–DER design of a two–subsystem interconnection based on a external DC link voltage regulation is tested by simulation and experimentation, feedback linearization (FL) without considering the system dynamic, FL considers that the dynamic system is evaluated to illustrate the performance of this approach.

The chapter is organized as follows. In section 1.2, the formulation of the energy transfer problem is given; in section 1.3, the Duindam–Stramigioli dynamic energy router is exposed; in section 1.4, the implementation and model of a Two–Port DS–DER is presented; in section 1.5, the simulation and experimental results of the DS–DER are shown; and in section 1.6, the chapter ends with some concluding remarks.

1.2 Formulation of the Energy Transfer Problem

In this section a concept of N multiports is modeled and considers that some energy blocks are interconnected between themselves in order to centralize references proposing certain nonlinear controllers in the dynamic behavior.

1.2.1 The Multiports

It is assumed that the multiports, denoted by Σ_j, $j \in \bar{N} := \{1, \ldots, N\}$, have as port variables the terminal voltages and currents, which we denote as $v_j(t), i_j(t) \in \mathbb{R}^{m_j}$, respectively (see Fig. 1.1). It is also assumed that the multiports satisfy the energy–conservation law

$$\text{Stored Energy} = \text{Supplied Energy} - \text{Dissipated Energy}.$$

The following scenario is considered.

(i) The stored energy is represented by a scalar function $\tilde{H}_j : \mathbb{R}^{n_j} \to \mathbb{R}$, whose argument $x_j(t) \in \mathbb{R}^{n_j}$ is the state vector of the multiport. In an electrical circuit, $x_j(t)$ consists of electric charges in the capacitors and magnetic fluxes in the inductors.

(ii) The power delivered by, or demanded from, the external environment is defined as

$$P_j(t) = v_j^\top(t) i_j(t), \tag{1.1}$$

with energy given by its integral.

(iii) The dissipated power is a non–negative function denoted $d_j : \mathbb{R}_+ \to \mathbb{R}_+$. For instance, the power dissipated in a linear resistive element R is given by

$$d(t) = R i_R^2(t),$$

where $R > 0$ is the value of the resistor and $i_R(t)$ is the current flowing through it.

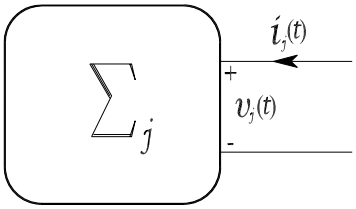

Figure 1.1: Representation of a subsystem, such as a fuel cell or battery, as a multiport, denoted by Σ_j, with port variables $v_j(t)$ and $i_j(t)$.

With this notation the energy–conservation law, in power form, becomes

$$\dot{H}_j(t) = P_j(t) - d_j(t), \tag{1.2}$$

where $H_j(t) := \tilde{H}_j(x_j(t))$. Integrating (1.1), and using (1.2), yields

$$H_j(t) - H_j(0) = \int_0^t v_j^\top(s) i_j(s) ds - \int_0^t d_j(s) ds.$$

Since $d_j(t) \geq 0$, we have

$$H_j(t) - H_j(0) \leq \int_0^t v_j^\top(s) i_j(s) ds, \tag{1.3}$$

reflecting the fact that the energy stored in the system cannot exceed the energy supplied from the environment, the difference being the dissipation.

Notice that, in order to be able to treat multiports with *sources*, we have not assumed that the energy function is positive definite, or bounded from below. For instance, the dynamics of an ideal battery is given by

$$\begin{aligned} \dot{x}_b(t) &= i_3(t) \\ v_3(t) &= \tilde{H}_b'(x), \end{aligned}$$

where $(\cdot)'$ denotes differentiation, and

$$\tilde{H}_b(x_b) = V_b x_b$$

is the (unbounded) energy, with $V_b \in \mathbb{R}_+$ the voltage of the battery. Clearly

$$H_b(t) = V_b \int_0^t i_3(s)ds,$$

is the energy extracted from the battery.

If the energy function $\tilde{H}(x)$ is positive definite, from (1.3) we obtain

$$-\int_0^t v_j^\top(s) i_j(s) ds \leq H_j(0),$$

stating that the energy *extracted* from the multiport is bounded (by the initial energy), which is the usual characterization of passive systems [20].

1.2.2 Criteria for current reference selection

The definition of the reference current $i_j^\star(t)$ described in section 1.4.1 can complement additional constraints aimed at satisfying, for example, instantaneous reactive power specifications in electrical power applications. In addition, and in order to discriminate between quickly and slowly changing power demands, the current reference might be filtered with lowpass, highpass, or bandpass filters before being sent to the power converter controller.

Due to the slow dynamics of fuel cells, in combined implementation with other sources, the current reference of the fuel cell port comes from the load current passed by a lowpass filter. As shown in Fig. 1.2, the sum of the current references of ports 1 and 2 is the current reference of port 3. In this way, the fast response of the supercapacitor is used to supply high power demands. Furthermore, in this particular example, the voltage terminals of the three ports are considered to have the same value; otherwise the current reference shape is given by

$$i_1 \frac{v_1}{v_3} + i_2 \frac{v_2}{v_3} = i_3.$$

1.3 The Duindam–Stramigioli Dynamic Energy Router

The operation of the DS–DER is briefly reviewed in this section, where dynamic energy transfer is a time–varying energy rate according to the operational energy needs of the system; for further details see [5].

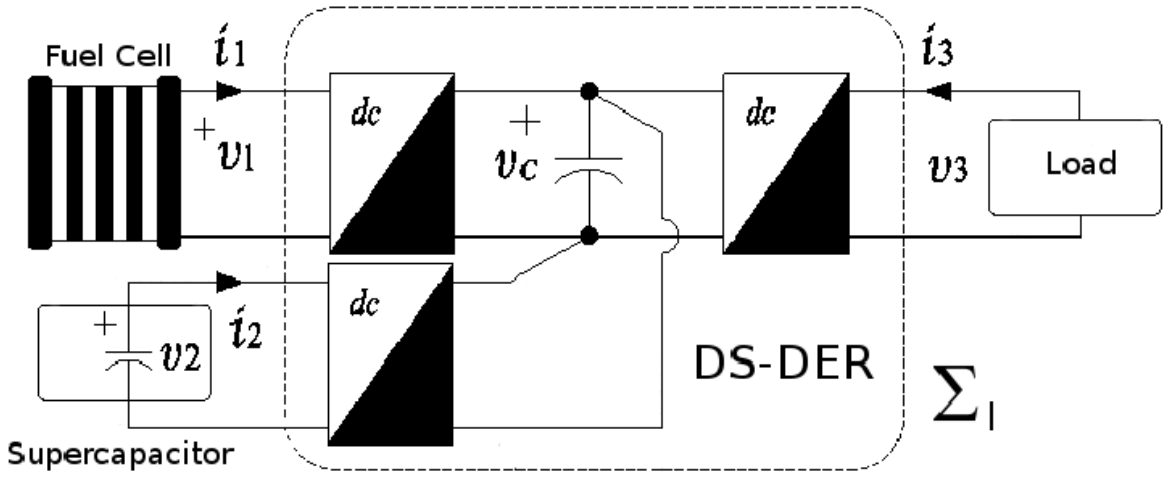

Figure 1.2: An example of current references in a multiport system with a fuel cell source unit, a supercapacitor as a storage unit, and a generic electric load. In this example, the current load experiences a fast increment.

For simplicity, we first consider, temporarily, the case of two multiports. Moreover, we are interested in energy–management applications where the dissipated energy is negligible, that is, $d_1(t), d_2(t) \approx 0$. Therefore, the power inequality (1.1) becomes

$$\begin{aligned} \dot{H}_1(t) &= \alpha(t)|v_1(t)|^2|v_2(t)|^2 \\ \dot{H}_2(t) &= -\alpha(t)|v_1(t)|^2|v_2(t)|^2. \end{aligned} \tag{1.4}$$

Assume that, at time $t \geq 0$, it is desired to instantaneously transfer energy from multiport Σ_1 to multiport Σ_2 without losses. Therefore, we require that

$$v_1^\top(t)i_1(t) + v_2^\top(t)i_2(t) = 0, \tag{1.5}$$

with

$$\dot{H}_1(t) > 0, \qquad \dot{H}_2(t) < 0. \tag{1.6}$$

Equation (1.6) ensures that $H_1(t)$ increases, while $H_2(t)$ decreases, as desired.

To accomplish the energy transfer objective, we couple the multiports through another multiport subsystem Σ_I, called the interconnection subsystem shown in Fig. 1.3. To satisfy the constraint (1.5), the device Σ_I must be lossless, that is, the total energy loss is zero; this condition is traditionally called *power–preserving*, which refers equivalently to the fact that the rate of energy loss is zero.

A lossless interconnection that satisfies (1.6) is the DS–DER, which is defined by

$$\begin{bmatrix} 0 & \alpha(t)v_1(t)v_2^\top(t) \\ -\alpha(t)v_2(t)v_1^\top(t) & 0 \end{bmatrix}, \tag{1.7}$$

therefore, the relation between the port variables is

$$\begin{bmatrix} i_1(t) \\ i_2(t) \end{bmatrix} = \begin{bmatrix} 0 & \alpha(t)v_1(t)v_2^\top(t) \\ -\alpha(t)v_2(t)v_1^\top(t) & 0 \end{bmatrix} \begin{bmatrix} v_1(t) \\ v_2(t) \end{bmatrix}, \tag{1.8}$$

where $\alpha(t) \in \mathbb{R}$ is a possibly time-varying designer–chosen parameter that, as shown below, controls the direction and rate of the energy flow change.

Multiplying (1.8) on the left by the row vector $\begin{bmatrix} v_1^\top(t) & v_2^\top(t) \end{bmatrix}$ yields (1.5). Hence, Σ_I is lossless. Furthermore, substituting the current expressions of (1.8) into (1.4) yields

$$\dot{H}_1(t) = \alpha(t)|v_1(t)|^2|v_2(t)|^2, \quad \dot{H}_2(t) = -\alpha(t)|v_1(t)|^2|v_2(t)|^2, \tag{1.9}$$

which shows that if $\alpha(t) > 0$, then (1.6) is satisfied. Note that the DS–DER ensures only that $H_1(t)$ is nonincreasing and $H_2(t)$ is nondecreasing. However, when the voltages are different from zero, which is the normal operating condition, the desired energy exchange occurs.

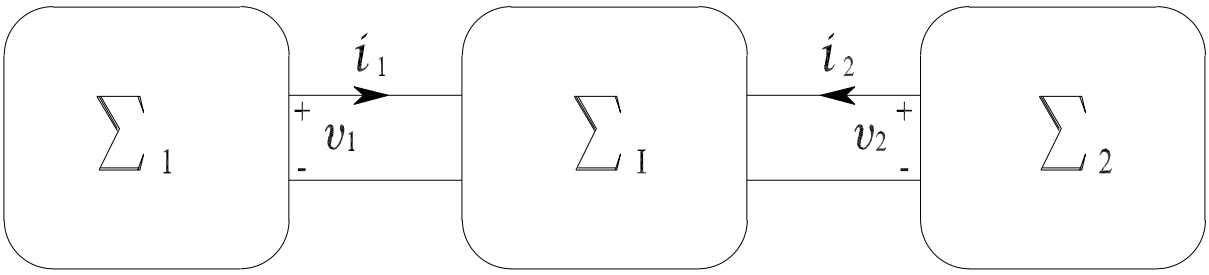

Figure 1.3: Interconnection subsystem, denoted by Σ_I. In order to couple multiports Σ_1 and Σ_2 satisfying the power preservation restriction, the interconnection subsystem must be lossless. The power–preserving interconnection Σ_I controls the energy–flow magnitude and direction.

The energy direction can also be inverted, that is, if $\alpha(t) < 0$, then the energy flows from Σ_2 to Σ_1. Moreover, the energy transfer rate can also be regulated with a suitable selection of $\alpha(t)$. For instance, regulating the rate of change of $\alpha(t)$, the energy flow can be made faster or slower thus providing the ability to comply with restrictions on time responses of the multiports. These features of the DS–DER are illustrated in the section 1.4.

The DS–DER defined by 1.8 is a current–tracking multiport. That is, given that $v_1(t), v_2(t)$, in 1.8 defines the desired values to be imposed on the multiport currents. A dual, voltage-tracking DS–DER can be defined as

$$\begin{bmatrix} v_1(t) \\ v_2(t) \end{bmatrix} = \begin{bmatrix} 0 & \alpha(t)i_1(t)i_2^\top(t) \\ -\alpha(t)i_2(t)i_1^\top(t) & 0 \end{bmatrix} \begin{bmatrix} i_1(t) \\ i_2(t) \end{bmatrix},$$

which yields

$$\dot{H}_1(t) = \alpha(t)|i_1(t)|^2|i_2(t)|^2, \quad \dot{H}_2(t) = -\alpha(t)|i_1(t)|^2|i_2(t)|^2.$$

The selection between current-tracking or voltage-tracking implementations of the DS–DER depends on technological considerations. In the current-tracking case, $\alpha(t)$ controls the direction and rate of change of the energy flow. Therefore, $\alpha(t)$ must be selected by considering the energy–exchange needs and physical constraints on the system, for example, the maximum current or voltage tolerated by the system.

A general form of the energy router is obtained considering the generic interconnected system

$$\begin{bmatrix} i_1(t) \\ i_2(t) \end{bmatrix} = \begin{bmatrix} 0 & \beta(t) \\ -\beta(t) & 0 \end{bmatrix} \begin{bmatrix} v_1(t) \\ v_2(t) \end{bmatrix}, \tag{1.10}$$

where the matrix $\beta(t) \in \mathbb{R}^{m\times m}$ is chosen such that the power conditions (1.6) are satisfied. Multiplying both sides of (1.10) by $\begin{bmatrix} v_1(t)^\top & v_2(t)^\top \end{bmatrix}$ yields

$$\begin{bmatrix} v_1^\top(t)i_1(t) \\ v_2^\top(t)i_2(t) \end{bmatrix} = \begin{bmatrix} v_1^\top(t)\beta(t)v_2(t) \\ -v_2^\top(t)\beta(t)v_1(t) \end{bmatrix}.$$

In the DS–DER, $\beta(t) = \alpha(t)v_1(t)v_2^\top(t)$, while alternative choices of this parameter are suitable for achieving the desired energy transfer, for example, the introduction of a saturation function in $\beta(t)$ is a technique for limiting the energy exchange between multiports. Therefore, a useful choice for energy management is

$$\beta(t) = \alpha(t)\phi_1(v_1(t))\left(\phi_2(v_2(t))\right)^\top,$$

where $\phi_i : \mathbb{R}^m \to \mathbb{R}^m$ are first–third quadrant mappings, that is, ϕ_i satisfies $a^\top\phi_i(a) > 0$ for all $a \in \mathbb{R}^m$. By suitable selection of these functions, it is possible to modulate the contribution of each multiport to the overall power delivered.

In the development above, it is assumed that the dissipated energy is negligible. More precisely, the dissipated energy in the resistors is assumed to be smaller than the energy transferred between the multiports, which is the case in many energy–management scenarios. The correct performance of the DS–DER cannot be ensured when this is not the case.

1.4 Implementation and Model of a Two-Port DS–DER

In this section, a DS–DER is implemented in two multiports Σ_1 and Σ_2, the configuration of the DS–DER was studied in [32], which have two supercapacitors by each port, interconnected via the DER as shown in Fig. 1.4. The energy functions of the supercapacitors

are represented by the following equation

$$\tilde{H}_j(v_j) = \frac{C_j}{2} v_j^2,\ j = 1, 2, \tag{1.11}$$

where C_j are the capacitances of the supercapacitors explained in [16], [17] and $v_j(t)$ their voltages. Their dynamics are described by

$$C_j \dot{v}_j(t) = -\frac{1}{R_C} v_j(t) + i_j(t), \quad j = 1, 2, \tag{1.12}$$

where $i_j(t)$ are the currents, and R_C is a parallel resistor.

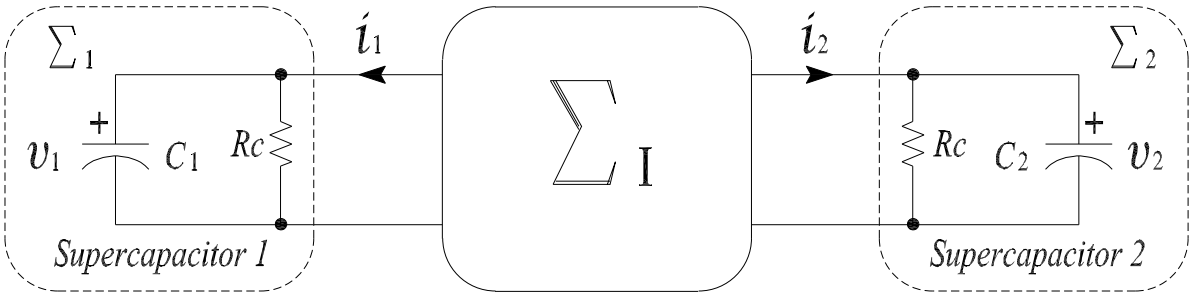

Figure 1.4: Interconnection of the multiports, chosen as leaky supercapacitors.

The power electronics scheme shown in Fig. 1.5 implements a two–ports DER. The port variables, $(v_i(t), i_i(t))$, $i = 1, 2$, are indicated on both sides of the bidirectional converter. Applying Kirchhoff's laws over the different switched states of the circuit, and assuming a sufficiently fast sampling time, the average dynamics of the DER interconnected to the multiports are given by

$$\begin{aligned} L_1 \frac{di_1}{dt}(t) &= -R_1 i_1(t) - v_C(t) u_1(t) + v_1(t) \\ L_2 \frac{di_2}{dt}(t) &= -R_2 i_2(t) - v_C(t) u_2(t) + v_2(t) \\ C_C \frac{dv_C}{dt}(t) &= u_1(t) i_1(t) + u_2(t) i_2(t), \end{aligned} \tag{1.13}$$

where $i_1(t), i_2(t)$ are the inductors currents, $v_C(t)$ is the voltage in the DC link, R_1, R_2, are the series resistances of the inductors, and $u_1(t), u_2(t) \in (0, 1)$ are the duty cycles of the switches, which are the control signals. The overall dynamics are, therefore, described by the fifth–order system (1.12) and (1.13).

The experimental setup is shown in Fig. 1.6. From left to right, we can see a black box with PWM modulator, behind it, the MOSFETS of the DER, for technical details see appendix A.2. On the right there is a box with the current sensors and next to it three inductors (round shaped) and two supercapacitors (blue). The battery lies below a big fuel cell in the back.

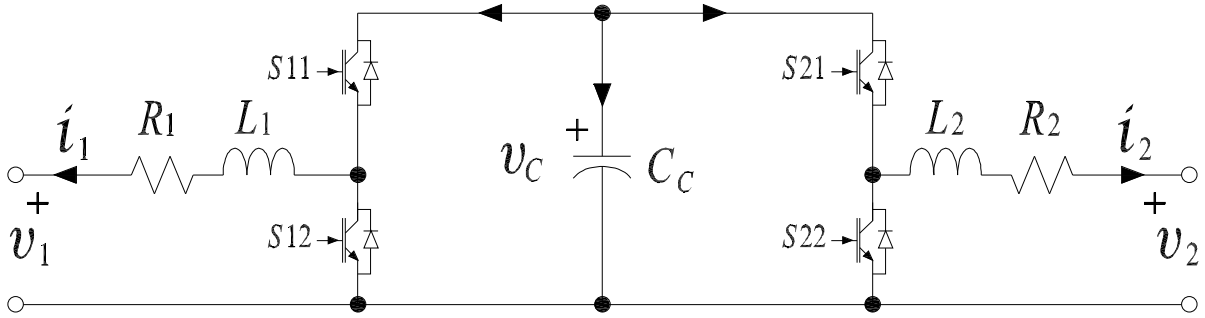

Figure 1.5: Power electronic configurations to implement a two–port DER.

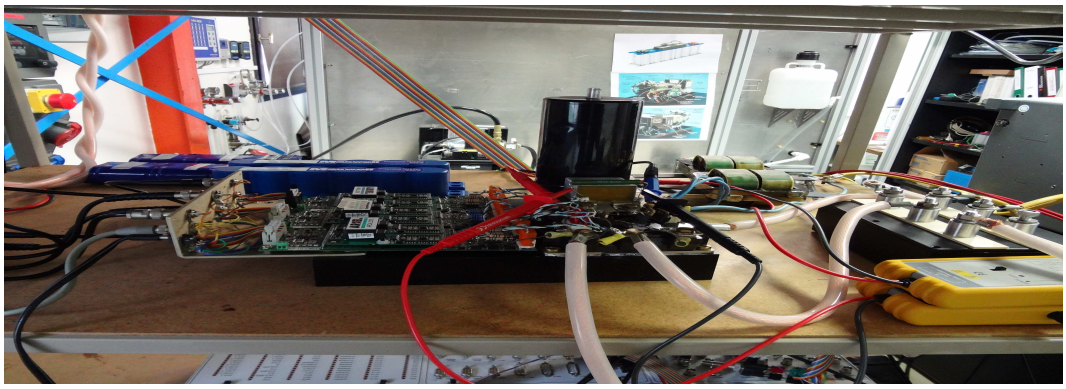

Figure 1.6: Photograph of the implemented test bench.

The nominal value of the DC link voltage is $v_C^\star = 20V$ and the initial voltage condition of $v_1(t)$ and $v_2(t)$ is $10V$. It is well known that, for a suitable operation of this kind of power electronic device, the voltage $v_C(t)$ should not decrease below a certain level [24], which in this case is about $17.5V$. All the parameters of the experimental implementation are shown in appendix A.1.

1.4.1 Energy management policy

To track the current references defined in (1.8) are designed with a profile of the function α(t) implemented this strategy,

$$\begin{bmatrix} i_1^\star(t) \\ i_2^\star(t) \end{bmatrix} = \begin{bmatrix} \alpha(t)v_1(t)v_2^2(t) \\ -\alpha(t)v_2(t)v_1^2(t) \end{bmatrix}, \tag{1.14}$$

where $i_1^\star$ and $i_2^\star$ are the desired port currents and α(t) is the time varying signal shown in Fig. 1.7. The same general shape of α(t) is used for our simulations and experiments, due to time computational restrictions, in the case of switched simulation, in experimentation, signal shift is expected due to the triggering of $\alpha(t)$. The variable $\alpha(t)$ can be constant or time varying, as shown in the plot.

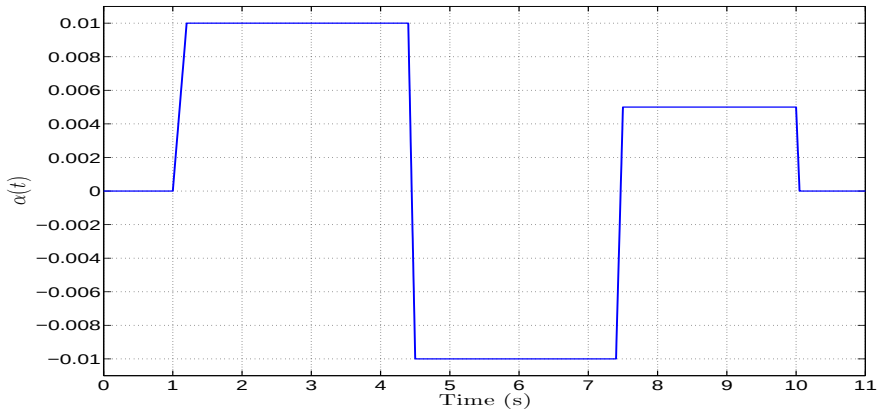

Figure 1.7: Time evolution of $\alpha(t)$, which controls the energy rate and direction.

In Fig. 1.7 the starting value of α(t) is zero, hence the energy exchange between C_1 and C_2 is null. At time 1 s, α(t) starts increasing at a constant rate and reaches the value 0.01 at 1.2 s. The variable α(t) remains at 0.01 for a 3.2 s period where the energy should be flowing from C_1 to C_2. At time 4.4 s, a decreasing ramp is imposed over α(t), ie, abrupt inversion of the sign of α(t) in the period between 4.4 s and 4.5 s. In order to recharge the supercapacitor C_1 with energy coming from C_2, the value of α(t) is kept at -0.01 until 7.4 s. In this instant, another abrupt change of α(t) (from -0.01 to 0.005) is produced in a period of 0.1 s. The signal α(t) remains at this value for 2.5 s, where once again, the energy should be flowing from C_1 to C_2, yet this time with half of the initial magnitude. In the final part of the profile of α(t), an instantaneous change of the signal is produced at time 10 s, where the signal change in the minimum possible time from 0.005 to 0 and remains at this value until the end of the test at 11 s.

1.5 Simulation and Experimental Results of the DS–DER

In this section, we tested three different nonlinear controls to implement the DS–DER for two ports. The results show here, were generated in both simulation and experimentation.

1.5.1 Current tracking via feedback linearization

The feedback linearization controller for the DS–DER is presented, using the dynamic (1.12) and (1.13), the controllers are design in the follow form,

$$u_1(t) = \frac{1}{v_C(t)}[v_1(t) - R_1 i_1(t) - L_1 \frac{di_1^*}{dt}(t) + L_1 \gamma \tilde{i}_1(t)], \quad (1.15)$$

$$u_2(t) = \frac{1}{v_C(t)}[v_2(t) - R_2 i_2(t) - L_2 \frac{di_2^*}{dt}(t) + L_2 \gamma \tilde{i}_2(t)], \quad (1.16)$$

where $\gamma > 0$ is a tuning parameter, and the tracking errors are defined by

$$\tilde{i}_1(t) = i_1(t) - i_1^\star(t), \quad \tilde{i}_2(t) = i_2(t) - i_2^\star(t).$$

Replacing (1.15) and (1.16) in the current equation (1.13), respectively, yields

$$\dot{\tilde{i}}_1(t) = -\gamma \tilde{i}_1(t), \quad \dot{\tilde{i}}_2(t) = -\gamma \tilde{i}_2(t), \quad (1.17)$$

which implies that the current–tracking errors converge to zero exponentially fast, at a rate determined by γ, to achieve the desired objective.

The derivatives of the reference currents used in (1.15) and (1.16) can be obtained using approximate differentiators. Alternative schemes that avoid differentiation can be derived from the results in [20, 21]. The control signals of the DS–DER, generated from (1.15) and (1.16), are the duty cycles of a PWM scheme operating at 20 kHz. The controller gain is set to $\gamma = 1000$. The derivatives of the current references are obtained by passing the signals through approximate differentiation filters

$$F_j(s) = \frac{k_j s}{\tau_j s + 1}, \ j = 1, 2.$$

where $k_j = 1$ and $\tau_j = 0.00003$. In order to keep the voltage v_C constant at $20V$, the same controller is implemented. Since this controller is based on the knowledge of the system, and the previous experimental results have proven that a deviation exists between the real and the simulation model of the system, an adjustment is done over the inductors series resistors in order to approximate the real losses of the whole circuit. Hence, the new chosen value for R_1 and R_2 is 0.27 Ω.

Simulation results of the DS–DER

The simulations shown in this subsection were carried out using Matlab Simulink, due to computational restrictions, an average simulation of 11 second was conducted. With these simulation results, it is possible to evaluate, for example, the performance of the approximate differentiation filter. A brief description of the figures are given.

Fig. 1.8 depicts the behavior of the instantaneous power and stored energy of Σ_1 and Σ_2, that is, $\dot{H}_1(t), H_1(t)$ and $\dot{H}_2(t), H_2(t)$, respectively. Fig. 1.8(a) illustrates that the power profile is achieved as desired, controlled by $\alpha(t)$ in both the direction and rate of change. Energy working conditions are shown in Fig. 1.8(b), the energy is being

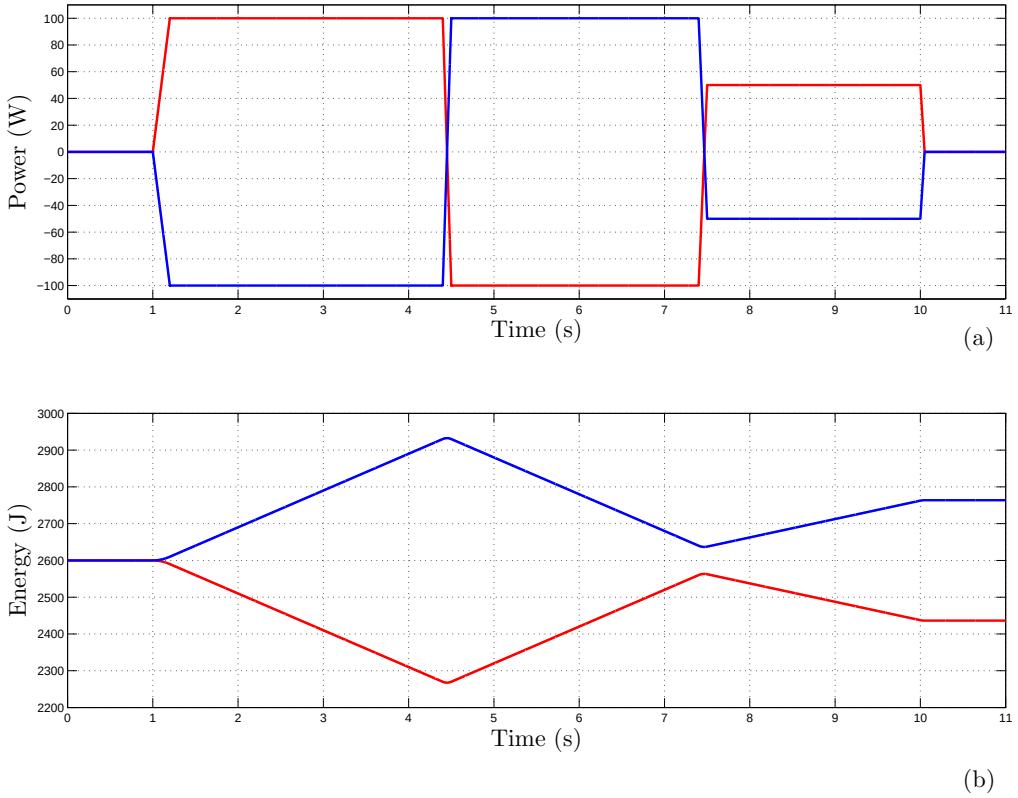

Figure 1.8: Simulation time evolution of the power and energy variation in ports 1 and 2. (a) Power $\dot{H}_1(t)$ and $\dot{H}_2(t)$ in red and blue, respectively. (b) Evolution of the energy stored $H_1(t)$) and $H_2(t)$ in red and blue, respectively, in the supercapacitors C_1 and C_2.

transferred from one capacitor to the other in a period of time from 1 s to 4.45 s, the energy stored in the capacitor C_2 is initially increasing, while the energy stored in the capacitor C_1 is decreasing. The opposite situation takes place in the period of time 4.45 s to 7.4 s.

In Fig. 1.9, v_C closely follows its reference (20 V) and only slight variations are produced during the changes of the α, ie, in the periods of time 1 s to 1.2 s, 4.4 s to 4.5 s, 7.4 s to 7.5 s, and at 10 s.

Experimental results of the DS–DER

Experiments are performed using the test bench shown in Fig. 1.6 to evaluate the behavior of the controller. Due to the experiment trigger in the dSPACE environment, α is shifted in relation to Fig. 1.7, yet the demanded magnitudes of power and energy are the same, therefore, the results are comparable with the simulations.

As is illustrated in Fig. 1.10, the power exchanged between the supercapacitors follows the same pattern of α and of the simulation results, yet there is a clear degradation of

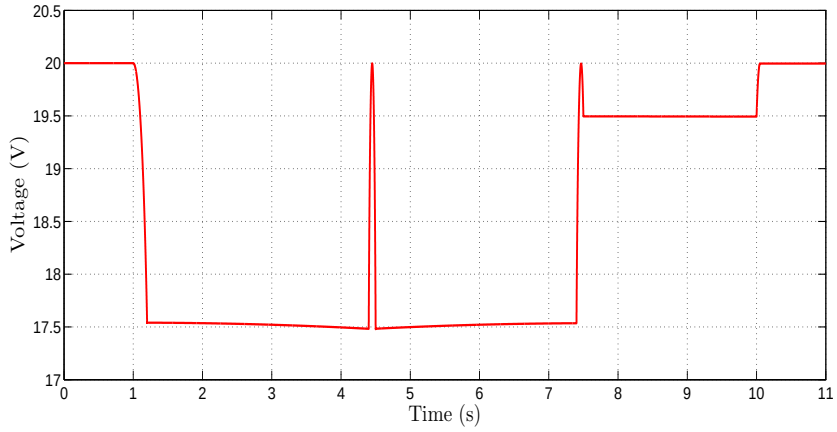

Figure 1.9: Simulation result from the time evolution of the DC link-voltage capacitor (v_C).

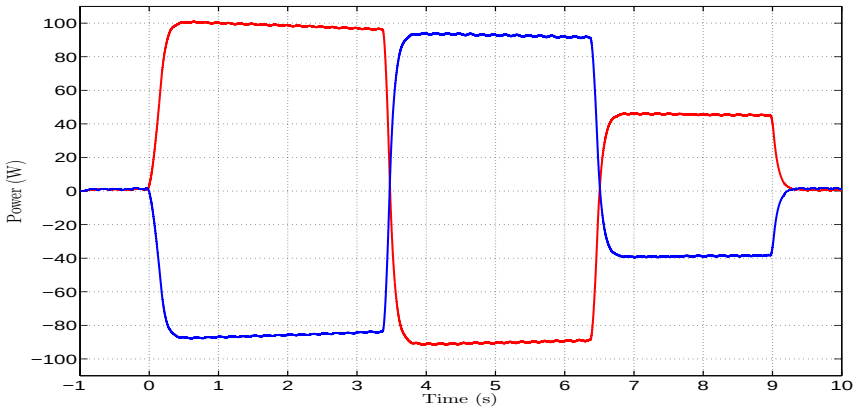

Figure 1.10: Experimental results for the feedback linearization control (1.15) and (1.16) of the power in ports Σ_1 and Σ_2. Power $\dot{H}_1(t)$ and $\dot{H}_2(t)$ in red and blue, respectively.

power signals. The tendency is appropriate, although the variation of power in the period of time 3.5 s to 6.9 s has been 10 W for C_1 and -10 W for C_2 that must be considered. In consequence, the difference of power has not been compensated for in the DS–DER. Similar to the power exchange, the energy had some variation.

There is a clear mismatch between i_1 and i_2, (shown in Fig. 1.11). In the period of time from 3.5 s to 3.6 s, there is a magnitude difference between i_1 and i_2 in a previous time 1 A average like variation, this tendency has been increasing as if it was to extend the work cycles. The fact is that at the end of the experimentation, ie, the period of time from 6.6 s to 9 s, the current mismatch increases (4.5 A for i_1 and -4 A for i_2), which means that the deviation of the signals from their references is caused by the inaccurate model of the system (with respect to the dissipation) used for the controller design.

In agreement with what is expected, the voltage of the DC link capacitor follows the

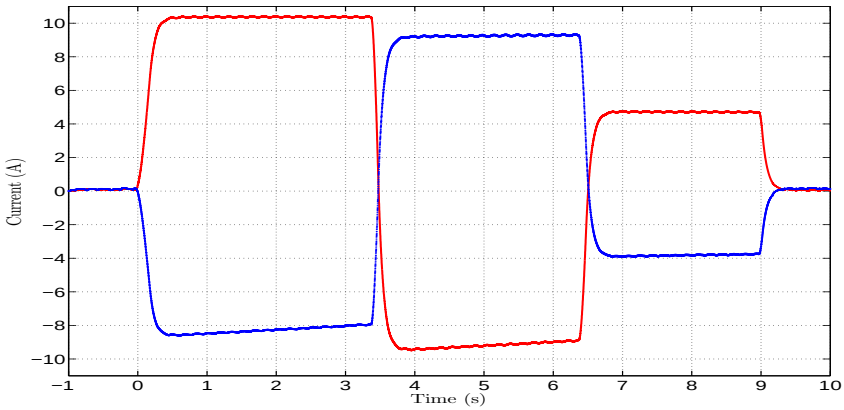

Figure 1.11: Experimental result for the feedback linearization control (1.15) and (1.16) of currents i_1, i_2. Current i_1 (red) and current i_2 (blue).

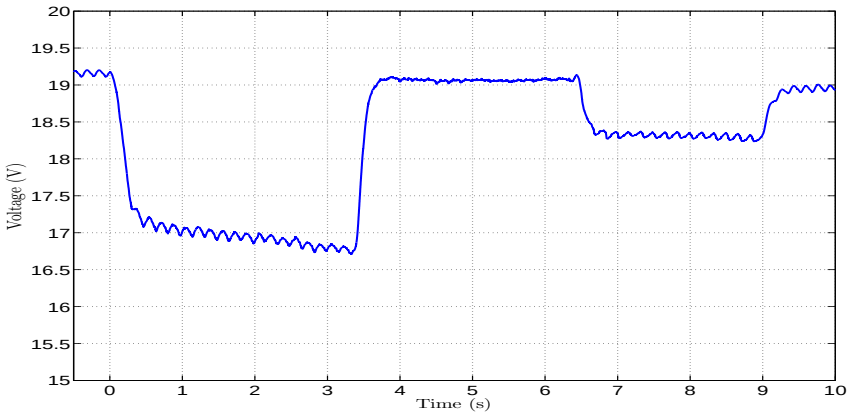

Figure 1.12: Experimental result for the feedback linearization control (1.15) and (1.16) of the DC link-voltage capacitor (v_C).

corresponding reference (19 V), its shape is presented in Fig. 1.12. As can be observed, and compared with previous results (figures 1.9), v_C presents a clear degradation (from the point of view of noise and/or ripple). In the first period of time from 0 s to 3.5 s, where the average energy exchange has a variation of 2 V , there is a clear difference between Fig. 1.9 and Fig. 1.12. It is possible that the losses are less in simulation than in experimental cases because the losses in the interconnection system are not considered so one of the multiports is supplying the dissipated energy, or the combination of both. It can be deducted that losses are supplied by one of the supercapacitors.

1.5.2 Current tracking via input–output linearization

Current tracking via input–output linearization is another technique that was tested in this subsection, the current references for the DS–DER defined in (1.8) can be rewritten

as,

$$\begin{bmatrix} i_1^\star(t) \\ i_2^\star(t) \end{bmatrix} = \begin{bmatrix} \alpha(t)v_1(t)v_2^2(t) \\ -\alpha(t)v_2(t)v_1^2(t) \end{bmatrix}.$$

The design is completed by adding a control strategy for the system (1.12), (1.13) that ensures the tracking of the current references. The problem of controller design for power converter systems has been extensively studied in the power electronics and control literature, see [20, 21, 24] and references therein. To remain as close as possible to the ideal tracking situation, it was assumed that the load dynamics are perfectly known, and an input–output linearization of the whole system was implemented. Toward this end, we take the tracking errors as system outputs,

$$\begin{aligned} \tilde{i}_1(t) &= i_1(t) - \alpha v_1(t)v_2^2(t) \\ \tilde{i}_2(t) &= i_2(t) + \alpha v_1^2(t)v_2(t), \end{aligned} \tag{1.18}$$

to drive their corresponding derivatives terms to zero, the next dynamic of (1.18) was follow,

$$\dot{\tilde{i}}_1(t) = \frac{di_1}{dt}(t) - \alpha v_2^2 \frac{dv_1}{dt}(t) - 2\alpha v_1 v_2 \frac{dv_2}{dt}(t), \tag{1.19}$$

$$\dot{\tilde{i}}_2(t) = \frac{di_2}{dt}(t) + \alpha v_1^2 \frac{dv_2}{dt}(t) + 2\alpha v_1 v_2 \frac{dv_1}{dt}(t). \tag{1.20}$$

Some simple calculations show that the system (1.12) and (1.13), with outputs (1.18) and inputs $u_1(t)$ and $u_2(t)$, has a well–defined relative degree of 1 and can be input–output linearized with the control law

$$\begin{aligned} u_1 &= \frac{L_1}{v_C}\left[\frac{-R_1 i_1 + v_1}{L_1} + \frac{\alpha v_2^2}{C_1}\left(i_1 + \frac{v_1}{R_{C1}}\right)\right] + \\ &\quad + \frac{L_1}{v_C}\left[\frac{2\alpha v_1 v_2}{C_2}\left(i_2 + \frac{v_2}{R_{C2}}\right) - w_1\right] \\ u_2 &= \frac{L_2}{v_C}\left[\frac{-R_2 i_2 + v_2}{L_2} - \frac{\alpha v_1^2}{C_2}\left(i_2 + \frac{v_2}{R_{C2}}\right)\right] - \\ &\quad - \frac{L_2}{v_C}\left[\frac{2\alpha v_1 v_2}{C_1}\left(i_1 + \frac{v_1}{R_{C1}}\right) - w_2\right], \end{aligned} \tag{1.21}$$

where, $w_1(t), w_2(t)$ are the new input signals. That is, the closed–loop system takes the simple linear form

$$\frac{d\tilde{i}_j}{dt}(t) = w_j(t), \quad j = 1, 2.$$

To complete the design, the new inputs $w_j(t)$ are taken as PI controllers around $\tilde{i}_j(t)$, that is,

$$w_j(t) = -k_{p_j}\tilde{i}_j(t) - k_{i_j}\int_0^t \tilde{i}_j(s)ds, \; j = 1, 2, \tag{1.22}$$

where k_{p_j}, k_{i_j} show some positive–tuning gains. This yields the exponentially stable dynamics

$$\frac{d^2\tilde{i}_j}{dt^2}(t) + k_{p_j}\frac{d\tilde{i}_j}{dt}(t) + k_{i_j}\tilde{i}_j(t) = 0, \quad j = 1, 2.$$

Experimental results of the DS–DER

In this subsection, the final results are presented of the input–output linearization control to the DS–DER. The power behavior of both ports are show in Fig. 1.13.

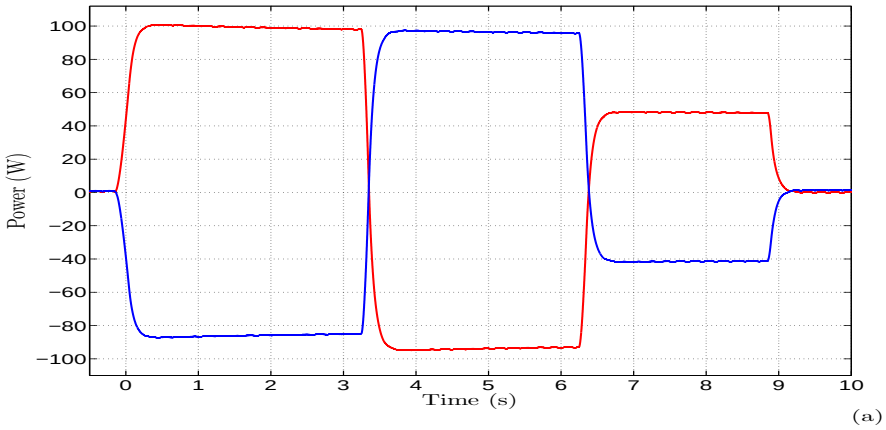

Figure 1.13: Experimental results of the DS–DER for the input–output linearization control (1.18)–(1.22) in a short–time window: a) $P_1(t)$, $P_2(t)$.

In a period of time 0 s to 3.4 s, the power follows a reference of 100 W though $\alpha(t)$ has a, average difference of 15 W in port 2, which means that port 1 sends the energy demanded for the controller, however, the power received by port 2 is less due to energy losses.

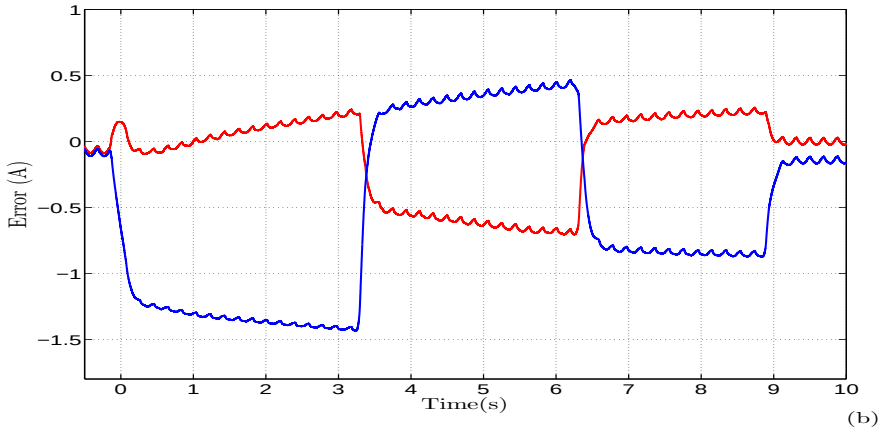

Figure 1.14: Experimental results of the DS–DER for the input–output linearization control (1.18)–(1.22) in a short–time window: b) $\tilde{i}_1(t)$, $\tilde{i}_2(t)$.

In cases of errors, Fig. 1.14 is interesting to show that $\tilde{i}_1(t)$ and $\tilde{i}_2(t)$ are minimums.

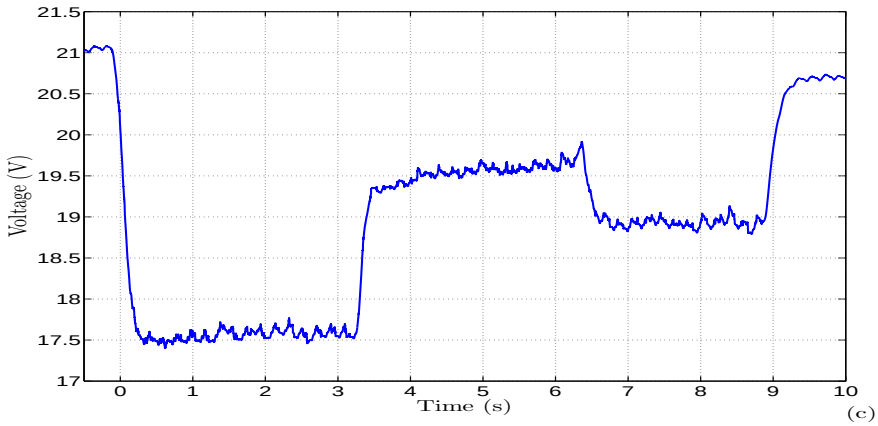

Figure 1.15: Experimental results of the DS–DER for the input–output linearization control (1.18)–(1.22) in a short–time window: c) $v_C(t)$.

The variation of $v_C(t)$ in Fig. 1.15 is bigger than the simulation of Fig. 1.9 because the initial condition voltage starts in a different stationary state.

1.5.3 Effect of dissipation on the DS–DER

The transient performance of the DS–DER with the input–output feedback linearizing controller (1.18)–(1.22) is depicted in Figs. 1.13, 1.14, and 1.15. As seen from the figure, the current tracking errors are kept small and the power transfer is done in the desired direction and requested rate of change. Moreover, the DC–link voltage, $v_C(t)$, is kept within reasonable values. However, we observed that since the dissipated power in the DER is not compensated, the values of the capacitor powers tend to decrease with time.

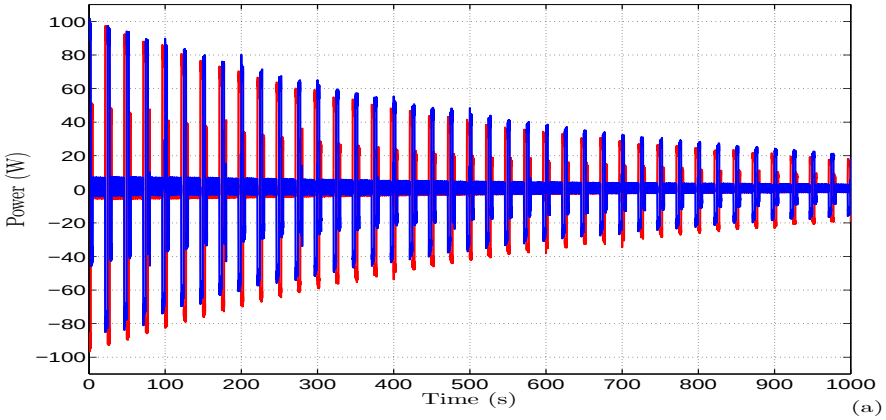

Figure 1.16: Experimental results of the DS–DER for the input–output linearization control (1.18)–(1.22) in a long–time window: a) $P_1(t)$, $P_2(t)$.

The power–loss trend is more clearly shown in Figs. 1.16, 1.17, and 1.18, which corresponds to a much longer experimentation time. Notice that the current tracking errors are still kept small,however, the DC–link voltage decreases to a level where the device ceases to be operational. This deleterious behavior was not observed in the simulations of [32] where a larger capacitor was used in the DC–link and the discharge time was much larger than the considered time horizon.

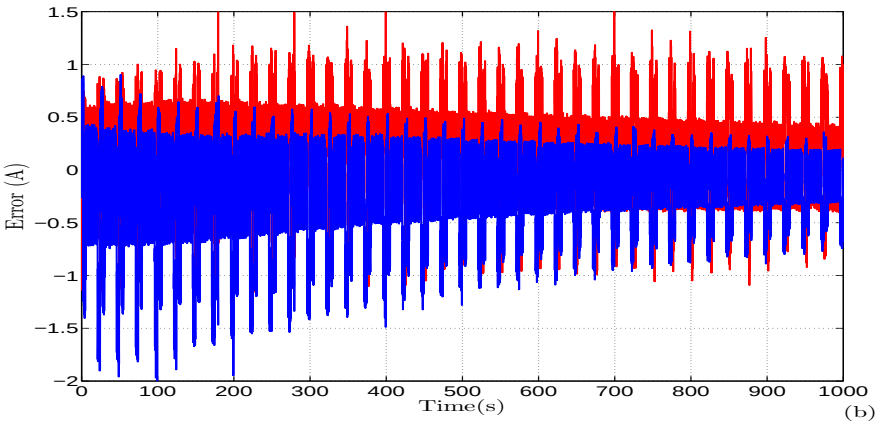

Figure 1.17: Experimental results of the DS–DER for the input–output linearization control (1.18)–(1.22) in a long–time window: b) $\tilde{i}_1(t)$, $\tilde{i}_2(t)$.

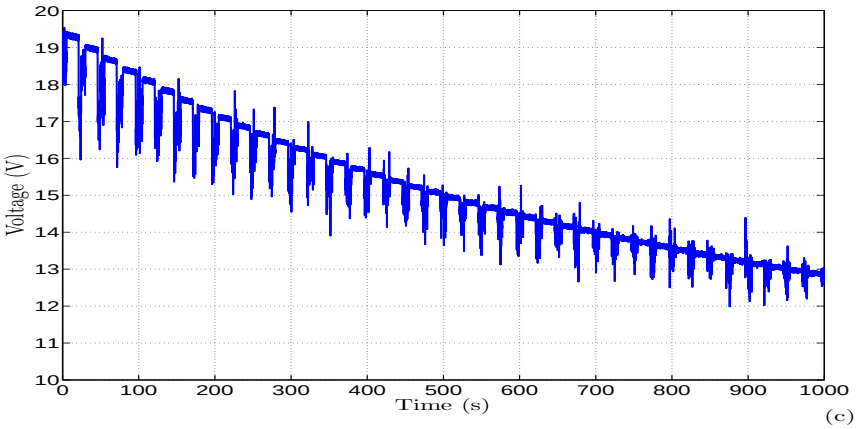

Figure 1.18: Experimental results of the DS–DER for the input–output linearization control (1.18)–(1.22) in a long–time window: c) $v_C(t)$.

1.6 Conclusions

A device to dynamically transfer energy between electrical multiports—the DS–DER—is presented and developed using standard switched power electronic devices. One of the

central features of the DS–DER is the ability to control the direction and magnitude of the energy flow by changing only the parameter $\alpha(t)$, which comes directly from power port considerations. The importance of directly controlling the energy flow in this interconnection is due to the ability to monitor the stocks as well as the consumption of energy in the various storage and source devices of the system. In an application of energy transfer involving batteries, it is essential to be aware of the energy level of the batteries before making decisions about the appropriate energy control policy. The performance of a nondissipative dual–port DS–DER for a dc–to–dc application was verified by both simulations and experiments. Moreover, a dissipative dual–port DS–DER was also tested by the same means. Three different controllers were evaluated in order to achieve the objectives and compare performance.

The performance of the DS–DER is in agreement with what was expected for a nondissipative interconnection, ie, the current references, obtained from the lossless interconnection matrix and the variable α(t), determine the energy exchange and the instantaneous power in each port.

The feedback linearization, without considering all the dynamics of the system, performed appropriately during simulation (good time response and tracking). Although, and due to the mismatch in the electrical model, the result of the experimentation was poor, mainly regarding steady state error. Due to this result, it was possible to realize that the adjustments of the model were not accurate enough and more precise studies should be done to consider the nonlinearities, and specifically, the dependency on the dissipative units (series or parallel resistance), and the operating point. Also, due to this implementation, it was possible to test (in simulation and experiment) the approximate differentiation filter. The outcome is that the performance is appropriate and extensive use of this technique should be done, mostly for tracking controllers.

Regarding the input–output linearization that introduces all the dynamics of the system, an ideal performance is observed in simulation, yet, during experimentation, the performance was slightly degraded. As in the previous case, the dependency of the controller the system parameters, impeded an ideal performance. Although, additional effort regarding controller design should imply meaningful improvements.

Finally, the power scheme without external energy supply yielded satisfactory results. The implemented control strategy (input–output linearization) enables the system to keep the DC–link voltage close to its reference by altering the energy exchange. Furthermore, the energy exchange magnitude is no longer defined only by alpha, ie, an increment is inserted on the energy flow in order to compensate for the losses. Due to this modification, the currents do not track the initial references and the DC–link voltage is no longer stabilized to its reference. Since the DC–link voltage control is a secondary objective of the control strategy, the fact that it was kept away from its reference does not impact the main goal of the DS–DER.

Chapter 2

New Dynamic Energy Router

2.1 Introduction

Achieving efficient transfer of electric energy between multidomain subsystems that can generate, store, or consume energy is a central problem in modern microgrid systems [33]. Depending on the operation regime, energy must be transferred between the various units which will be referred to as multiports according to some energy–management policies. The energy exchange between the multiports is achieved by interconnecting them through power converters, which are electronically–switched circuits capable of adjusting the magnitudes of the port variables, voltage, or current, to a desired value.

To achieve the desired energy–management policy, it is common practice to assume that the system operates in steady state and then translates the power demand (flow sense and magnitude) for each multiport into current or voltage references–see, [22], [23], [30], and [31]. These references are then tracked with control loops, usually proportional plus integral (PI). Since the various multiports have different time responses, it is often necessary to discriminate between quick and slow changing power–demand profiles. For instance, due to physical constraints, it is not desirable to demand quick changing power profiles to a fuel–cell unit. Hence, the peak demands of the load are usually supplied by a bank of supercapacitors, whose time response is fast. To achieve this objective, a steady–state viewpoint was again adopted, and the current or voltage references to the multiports are passed either through lowpass or highpass linear time–invariant (LTI) filters.

The steady–state approach currently adopted in practice can only approximately fulfill the desired objectives of energy transfer and slow–versus–fast discrimination of the power demand. In particular, during the transients or when a fast dynamic response is required, the delivery of the demanded power in response to current or voltage references and the time response action of the filters might be far from satisfactory.

Following the principles of Control-by-Interconnection [34], a new strategy to dynamically control the energy flow between *lossless* multiports, together with its corresponding

power electronics implementation, and standard circuit topologies was proposed in [32]. The device was called Duindam–Stramigioli Dynamic Energy Router (DS–DER) because, on one hand, it is inspired by the conceptual energy discrimination idea proposed, in the context of walking robots, in [13]. On the other hand, in contrast with current practice, it does not rely on steady–state considerations. The DS–DER generates, via a nonlinear transformation, the references (voltages or currents) of *all* multiports that, under the assumptions of perfect tracking, ensures *instantaneous* energy transfer among multiports.

As explained in [32], the flow direction and rate of energy transfer change are regulated by means of some free parameters, which in the simplest two multiport case reduces to a single scalar function. The selection of these parameters is rather intuitive, and replaces the time–consuming task of selecting the LTI filters that (approximately) enforce the desired time–scale separation between the multiports. Another feature that distinguishes the DS–DER from current practice is that, since the references of all interconnected multiports are generated in a centralized manner, information exchange among them is required—which is the operating scenario in some modern energy transfer applications.

A key assumption for the correct operation of the DS–DER proposed in [32] is that both the multiports and the DER itself are ideal lossless devices. Unfortunately, in this chapter it is shown that in the presence of dissipation—which is, obviously, unavoidable in applications—the energy of the DER monotonically decreases leading to an improper behavior, and eventually total dysfunction, of the DS–DER. There are three objectives of this chapter:

(1) To propose a modified DER that overcomes this fundamental problem, with guaranteed stability properties.

(2) To compare via experiments and simulations, the performances of the new DER and the DS–DER.

(3) To show that adding an outer–loop PI to the DS–DER with a switch that determines the direction of the energy flow, provides excellent simulation and experimental results. As usual with simple engineering intuition–based control schemes, no theoretical basis for the performance improvement of this so called directional DER can be provided.

The chapter is organized as follows. In section 2.2, the reformulation of the energy transfer problem is presented. Section 2.3 is devoted to the implementation and modeling of a Three–Port DER. While in section 2.4, simulation and experimental results of the New DER are exposed. Ad-hoc modification to the DS–DER, in section 2.5, is shown. The chapter ends with some concluding remarks in section 2.6.

2.2 Reformulation of the Energy Transfer Problem

In this section, the mathematical reformulation of the problem observed in chapter 1 is given for the new dynamic energy router (DER). Reconsidering the system composed of N multiports interconnected via (switch–regulated) power converters, we address the problem, once again, of energy exchange according to a prespecified energy–management policy.

2.2.1 Standard energy management procedure

The typical procedure to achieve energy transfer is as follows in [22] and [31]. Assume that at a given time $t_0 \geq 0$, a demand $P_j^\star$ of power is requested from multiport Σ_j, where Σ_j, $j \in \bar{N} := \{1, \ldots, N\}$. Measuring the voltage $v_j(t_0)$, the power demand is then transformed into a *constant* current reference $i_j^\star$, solving the instantaneous power relation.

$$P_j^\star = v_j^\top(t_0) i_j^\star. \tag{2.1}$$

This current reference is imposed on the controller that regulates the switches of the corresponding power converter, usually a PI loop, to drive the current error to zero $i_j(t) - i_j^\star$; In this way, the desired energy–transfer objective is achieved asymptotically–provided that the presumed steady–state behavior did not change.

The following observations regarding the aforementioned strategy are in order. First, regulation towards the desired current value $i_j^\star$ is, of course, not instantaneous, and during the transient, the voltage $v_j(t)$ will change. Consequently, the actual power extracted (or supplied) to the multiport Σ_j will, in general, not coincide with $P_j^\star$. Second, the strategy is intrinsically decentralized and neglects the loading effects that appear due to the interconnection of the multiports. To partially overcome this drawback, a second supervisory level of control is added to achieve the coordination between the multiports power demands—whose successful operation relies on time–scale separation assumptions that are, partially, enforced via filtering. Both shortcomings are, to a certain point, palliated by the DER.

2.2.2 The interconnection system

For the DER, the various power converters interconnecting the multiports are grouped together. It then defines a dynamic system that states $\xi \in \mathbb{R}^{n_I}$, energy function $\tilde{H}_I : \mathbb{R}^{n_I} \to \mathbb{R}_+$ and N port variables $v_{Ij}(t), i_{Ij}(t) \in \mathbb{R}^{m_j}$ that, being a physical system, also satisfies the energy conservation law

$$\dot{H}_I(t) = \sum_{j=1}^{N} v_{Ij}^\top(t) i_{Ij}(t) - d_I(t), \tag{2.2}$$

where $H_I(t) := \tilde{H}_I(\xi(t))$ and $d_I : \mathbb{R}_+ \to \mathbb{R}_+$ is the dissipation.

The multiports and the power converter device are coupled via the power–preserving interconnection

$$\begin{bmatrix} i_j(t) \\ v_j(t) \end{bmatrix} = \begin{bmatrix} 0 & -I_{mj} \\ I_{mj} & 0 \end{bmatrix} \begin{bmatrix} v_{Ij}(t) \\ i_{Ij}(t) \end{bmatrix}. \tag{2.3}$$

See Fig. 2.1. Defining the energy of the overall system

$$H_T(t) = \sum_{j=1}^{N} H_j(t) + H_I(t),$$

yields the power balance

$$\dot{H}_T(t) = -d_I(t) - \sum_{j=1}^{N} d_j(t).$$

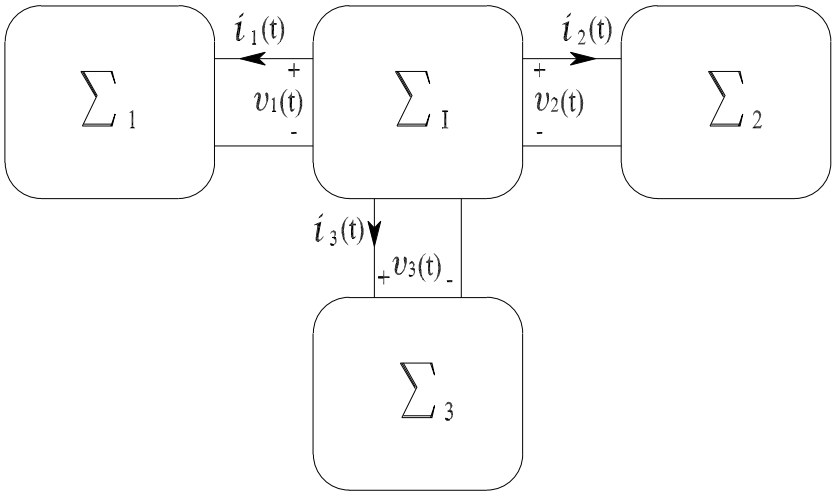

Figure 2.1: Overall interconnected system for $N = 3$.

2.2.3 A DER with losses compensation

To overcome the limitations mentioned in the previous chapter, we propose to design the DER taking into account the presence of the dissipation in the interconnection subsystem $d_I(t)$, which we assume is *measurable*. Notice that, since the DER is composed of the power converters, a good estimate of the resistive elements is available.

To streamline the problem formulation, we define N mappings $F_j : \mathbb{R}^r \to \mathbb{R}^{m_j}$, where $r := \sum_{j=1}^{N} m_j$, and the vectors

$$v := \text{col}(v_1, \ldots, v_N),\ F(v) := \text{col}(F_1(v), \ldots, F_N(v)).$$

The mappings $F_j(v)$ define the current references as

$$i_j^\star(t) = F_j(v(t)), \quad j \in \bar{N},$$

and they should meet two different objectives. First, to ensure the desired power dispatch, they should satisfy

$$P_j^\star(t) = v_j^\top(t) F_j(v(t)),$$

where $P_j^\star : \mathbb{R}_+ \to \mathbb{R}$ is the power that we want to extract (or provide) to the j–th multiport—this information comes from a higher level energy dispatch system. Second, to compensate for the dissipation in the DER, the mappings should satisfy

$$\sum_{j=1}^{N} v_j^\top(t) F_j(v(t)) = d_I(t). \tag{2.4}$$

Indeed, from (2.2) and (2.3), it is clear that if $i_j(t) \to i_j^\star(t)$, then the energy of the DER is regulated at a constant value, *ie*, $\dot{H}_I(t) \to 0$, which avoids the discharge phenomenon of the DS–DER.

A geometric interpretation of the new DER formulation and the DS–DER is given in Figs. 2.2 and 2.3, respectively. Given a voltage vector v and the dissipation d_I, the set F in Fig. 2.2 defines the admissible vectors $F(v)$, that satisfy (2.4). The figure shows two particular choices, which correspond to $P_1^\star < 0$ and $P_1^\star > 0$, respectively. In the case of the DS–DER (1.8), that using the notation above, takes the form

$$F(v) = \begin{bmatrix} \alpha v_1 |v_2|^2 \\ -\alpha v_2 |v_1|^2 \end{bmatrix},$$

where the set F is orthogonal to v, as shown in Fig. 2.3.

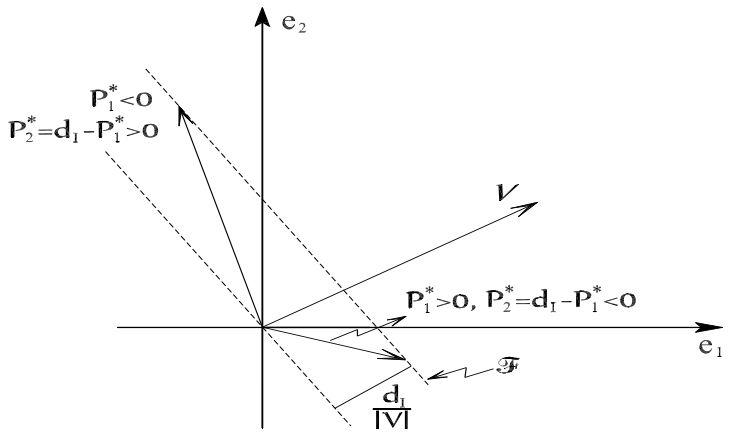

Figure 2.2: Geometric interpretation of the new DER for $N = 2$.

A possible choice for the mappings $F_j(v)$ is given by

$$F_j(v) = \delta_j \Pi_{k=1, k\neq j}^{N} |v_k|^2 v_j, \tag{2.5}$$

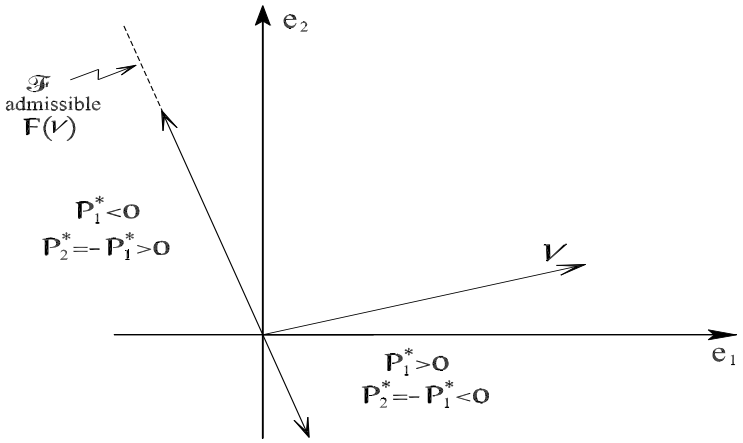

Figure 2.3: Geometric interpretation of the Duindam–Stramigioli DER for $N = 2$.

where $\delta_j : \mathbb{R}_+ \to \mathbb{R}$ are functions, chosen by the designer that, besides meeting the desired power dispatch policy, should satisfy

$$\sum_{j=1}^{N} \delta_j(t) = d_I(t).$$

Given the clear geometric interpretation of the DER, it is our contention that a suitable selection of the coefficients $\delta_j(t)$ is simpler than the choice of the LTI filters in standard practice, see [32].

If the multiport voltages are bounded away from zero, that is $|v_j(t)| \geq \epsilon > 0$, the coefficients $\delta_j(t)$ may be selected as follows. Fix the desired power of $N-1$ multiports $P_j^\star(t)$, and assign to the N–th multiport the task of compensating for $d_I(t)$.That is, define

$$P_N^\star(t) := d_I(t) - \sum_{j=1}^{N-1} P_j^\star(t). \tag{2.6}$$

For $j = 1, \ldots, N-1$, let

$$\delta_j(t) := \frac{P_j^\star(t)}{\Pi_{k=1}^N |v_k(t)|^2}$$

while we fix

$$\delta_N(t) := \frac{1}{\Pi_{k=1}^N |v_k(t)|^2} \left(d_I(t) - \sum_{j=1}^{N} P_j^\star(t) \right).$$

In this way, we (asymptotically) ensure the desired power dispatch is reached, $i_j^\top(t) v_j(t) \to P_j^\star(t)$, while, at the same time, the energy of the DER regulate.

Clearly, this strategy simply reduces to

$$F_j(v_j(t)) = \frac{P_j^\star(t)}{|v_j(t)|^2} v_j(t), \tag{2.7}$$

which is the solution of the time–varying version of equation (2.1) that corresponds to the current $i_j^\star(t)$ of smallest amplitude that delivers the desired power. It should be underscored that, besides the somehow minor fact that we are now generating time–varying references for the currents, another fundamental difference between the proposed DER and current practice is that *all* references are generated simultaneously.

2.2.4 Energy management policy for the new DER

The following energy management scenario for the DER was considered.

- In the interval $0 \leq t < 1$ s, there is no energy exchange between the multiports, which corresponds to $P_1^\star = P_2^\star = 0$ W.

- At $t = 1$ s, a slow transfer of energy from Σ_1 to Σ_2 is requested, and this remains until $t = 4.4$ s, at a power rate $P_1^\star = 100$ W.

- For $t > 4.4$ s a quick reversal of the energy flow is desired, remaining unchanged until $t = 7.4$ s, now at a power rate $P_2^\star = 100$ W.

- For $t > 7.4$ s another quick reversal of the energy flow is desired, remaining unchanged until $t = 10.05$ s, but now at half the preceding power value; that is $P_1^\star = 50$ W.

- Finally, for $t > 10.05$ s, the energy flow is instantaneously stopped until the end of the trial at $t = 11$ s.

A profile of the function $\alpha(t)$ that implements this strategy is shown in Fig. 2.4. Notice that the first slope is smaller than the second and third, reflecting the desire to carry out a slower energy transfer. On the other hand, the fourth slope, at $t = 10.05$ s, is very large to implement a quick stop of the energy transfer. The numerical values of $\alpha(t)$ are computed, using (1.4) with the nominal voltages, to deliver the desired powers indicated above.

2.3 Implementation and Model of a Three–Port DER

The power electronics scheme shown in Fig. 2.5 implements the three ports of the DER with the aforementioned battery.

The average dynamics of the circuit, terminated with the supercapacitors and the battery, now includes a third state and a third control signal, and are given by

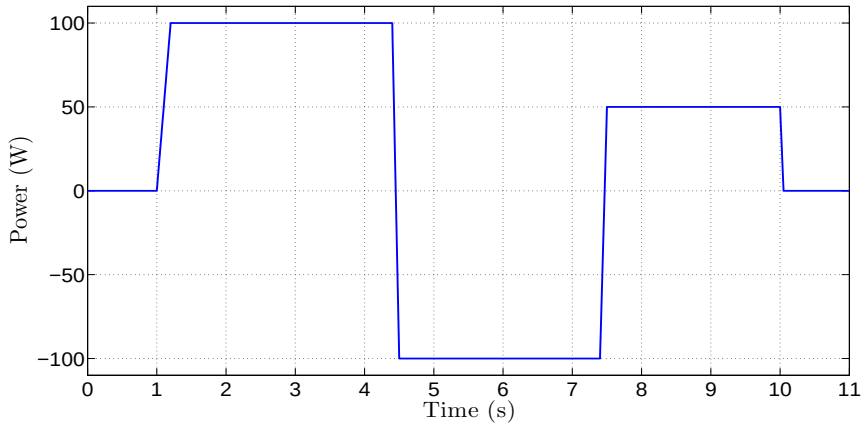

Figure 2.4: Time evolution of $P_1^{\star}(t)$, which controls the energy direction and exchange rate.

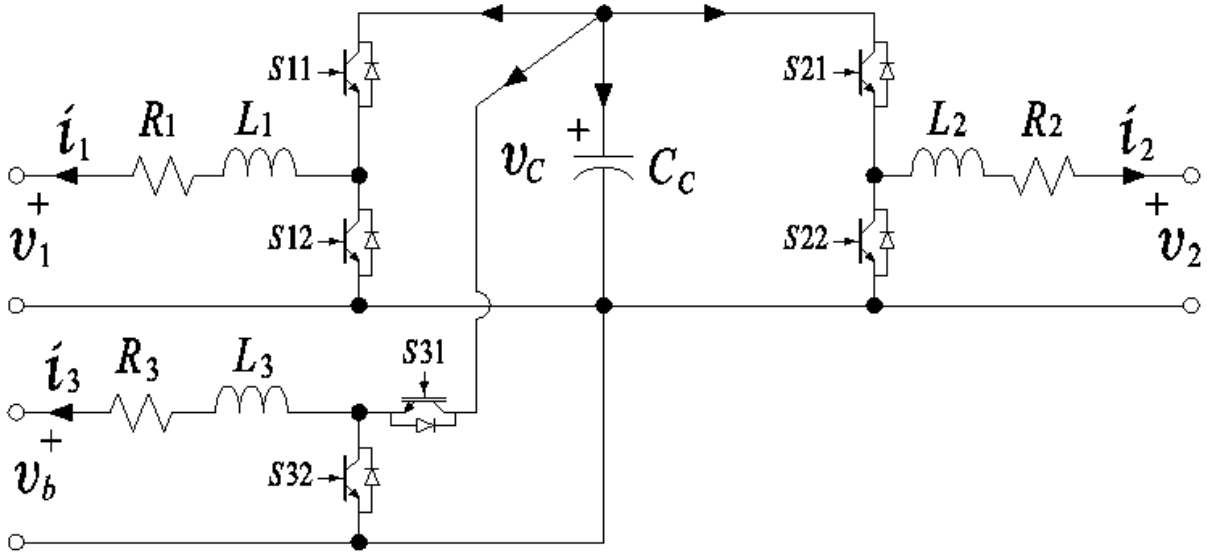

Figure 2.5: Power electronics implementation of the new DER router with a battery as a third multiport.

$$L_1 \frac{di_1}{dt}(t) = -R_1 i_1(t) - v_C(t)u_1(t) + v_1(t), \tag{2.8}$$

$$L_2 \frac{di_2}{dt}(t) = -R_2 i_2(t) - v_C(t)u_2(t) + v_2(t), \tag{2.9}$$

$$L_3 \frac{di_3}{dt}(t) = -R_3 i_3(t) - v_C(t)u_3(t) + v_3(t), \tag{2.10}$$

$$C_C \frac{dv_C}{dt}(t) = u_1(t)i_1(t) + u_2(t)i_2(t) + u_3(t)i_3(t), \tag{2.11}$$

where $i_1(t)$ and $i_2(t)$ are the inductor currents, $v_C(t)$ is the voltage in the DC–link capacitor and $u_1(t)$ and $u_2(t)$, $\in (0, 1)$ are the duty cycles of the switches, which represent

the control signals. The specified resistance (R_1 and R_2 are the series resistance of the inductors, $i_3(t), v_3$ are the current and voltage of the third port (the battery), and $u_3(t) \in (0,1)$ is the duty cycle of the additional switch. In order to be able to treat multiports with *sources*, we have not assumed that the energy function is positive definite or bounded from below. The dynamic of an ideal battery is given by

$$\begin{aligned} \dot{x}_3(t) &= i_3(t) \\ v_3(t) &= V_b, \end{aligned}$$

where $V_b \in \mathbb{R}_+$ is the voltage of the battery. The overall dynamics of the DER interconnected to the multiports are then given by the sixth–order system (2.14), (2.15), and (2.8)–(2.11) with $v_3(t) = V_b$.

The chosen subsystems connected to ports 1 and 2 are supercapacitors (C_1 and C_2), which model contains a parallel resistor R_C. For model and simulation purpose, the capacitors and resistors are considered linear. Supercapacitors are used as storage devices, its capacitance is in the order of hundreds of Faraday, on the other hand, the parallel resistances have magnitudes of mega-ohms. Capacitance on the order micro-Faraday are used for voltage regulation.

The energy functions of the multiports are

$$H_1(t) = \frac{C_1}{2} v_1^2(t), \tag{2.12}$$

$$H_2(t) = \frac{C_2}{2} v_2^2(t). \tag{2.13}$$

Their dynamics are described by

$$C_1 \dot{v}_1(t) = -i_1(t) - \frac{1}{R_C} v_1(t), \tag{2.14}$$

$$C_2 \dot{v}_2(t) = -i_2(t) - \frac{1}{R_C} v_2(t), \tag{2.15}$$

where C_1, v_1, and i_1 are the capacitance, voltage, and current of port 1 and C_2, v_2 and i_2 are the capacitance, voltage, and current of port 2. An experimental test bench is implemented to evaluate the performance of the new DER, the interconnection of three multiports corresponds to the power electronics implementation is shown in Fig. 2.5. The experimental setup is shown in Fig. 2.6, in the upper part from the right of this experimental desk, two supercapacitors (blue) can be seen, three inductors to the left of the supercapacitors, and the current (yellow boxes) and voltage sensors (one black box). In the left part of the desk are the power converter and the switch drivers, with its corresponding power supply under the desk.

The nominal value chosen for v_C is 20 V and the initial voltage condition for v_1 and v_2 are 10 V each. Experimental implementation parameters used for simulation purposes, are presented in Table 2.1.

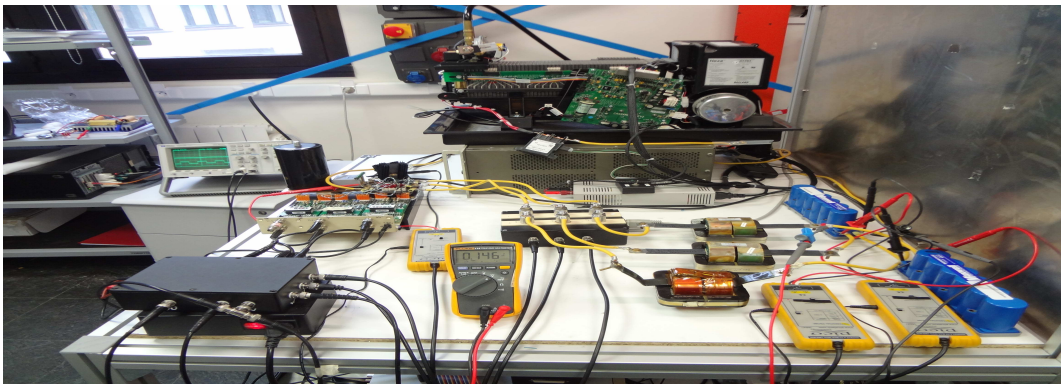

Figure 2.6: Test bench photograph of three ports.

Table 2.1: Power electronics implementation parameters.

Element	Value
L_1, L_2, and L_3	195 μH
R_1, R_2, and R_3	0.01 Ω
C_1, C_2	52 F
C_C	1.05 mF
R_C	1 M Ω
V_b	12 V
$SwitchingFrequencies$	20 kHz

Three different control strategies are developed and evaluated via simulation and experimentation. The problem of controller design for power converter systems of the form described by (2.8), (2.9), (2.10), and (2.11) is in the power electronics and control literature [20, 21, 24].

2.3.1 Linearized system of three ports

The block diagram of the general control scheme is the one depicted in Fig. 2.7, the strategy works as follows:

- PI controller of port 1 drives the error to zero between i_1 and i_1^*, the reference comes from the first term in (2.7).
- PI controller of port 2 drives the error to zero between i_2 and i_2^*, in the same way as before, the reference comes from the second term in (2.7).
- PI controller of port 3 drives the error to zero between i_3 and i_3^*. The reference of the battery current comes from the output of the DC link-voltage controller (PI controller of v_C), where the chosen DC link-voltage reference is $v_C^* = 20$ V.

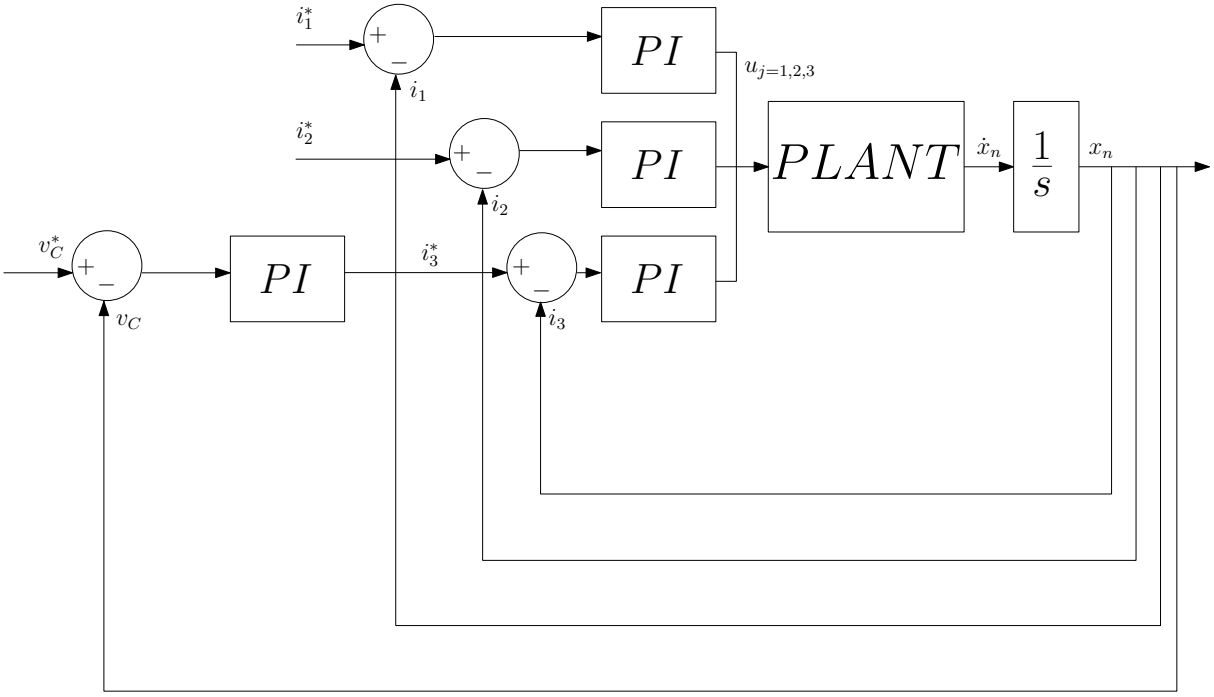

Figure 2.7: Control scheme of the DS–DER using linear PI controllers to follow the current references.

The controller design is accomplished by using linear–control techniques [28], [27]; therefore, the first step is to obtain the linearized system around the operation point of a nonlinear system,

$$\dot{x} \;=\; f(x,u), \tag{2.16}$$

the matrices A and B, near the operating point will be

$$\frac{\partial f}{\partial x}|_{x=\bar{x}} \;=\; A,$$

$$\frac{\partial f}{\partial u}|_{x=\bar{x}} \;=\; B,$$

the dynamic of each state variable is represented by $\tilde{x} = \mathrm{col}(\tilde{i}_1, \tilde{i}_2, \tilde{i}_b, \tilde{v}_1, \tilde{v}_2, \tilde{v}_C)$, and their new inputs as $\tilde{u} = \mathrm{col}(\tilde{u}_1, \tilde{u}_2, \tilde{u}_3)$. The linearized model of the system is,

$$\dot{\tilde{x}} \;=\; \left[\; A \;\right]\tilde{x} + \left[\; B \;\right]\tilde{u} + \left[\; C \;\right], \tag{2.17}$$

where,

$$\left[\ A\ \right] = \begin{bmatrix} \frac{-R_1}{L_1} & 0 & 0 & \frac{1}{L_1} & 0 & \frac{-\bar{u}_1}{L_1} \\ 0 & \frac{-R_2}{L_2} & 0 & 0 & \frac{1}{L_2} & \frac{-\bar{u}_2}{L_2} \\ 0 & 0 & \frac{-R_b}{L_b} & 0 & 0 & \frac{-\bar{u}_3}{L_b} \\ \frac{-1}{C_1} & 0 & 0 & \frac{-1}{R_C C_1} & 0 & 0 \\ 0 & \frac{-1}{C_2} & 0 & 0 & \frac{-1}{R_C C_2} & 0 \\ \frac{\bar{u}_1}{C_C} & \frac{\bar{u}_2}{C_C} & \frac{\bar{u}_3}{C_C} & 0 & 0 & 0 \end{bmatrix}, \tag{2.18}$$

$$\left[\ B\ \right] = \begin{bmatrix} \frac{-\bar{v}_C}{L_1} & 0 & 0 \\ 0 & \frac{-\bar{v}_C}{L_2} & 0 \\ 0 & 0 & \frac{-\bar{v}_C}{L_b} \\ 0 & 0 & 0 \\ 0 & 0 & 0 \\ \frac{\bar{i}_1}{C_C} & \frac{\bar{i}_2}{C_C} & \frac{\bar{i}_b}{C_C} \end{bmatrix}, \tag{2.19}$$

$$\left[\ C\ \right] = \begin{bmatrix} 0 \\ 0 \\ \frac{v_b}{L_b} \\ 0 \\ 0 \\ 0 \end{bmatrix}, \tag{2.20}$$

thus, $\bar{i}_1$, $\bar{i}_2$, $\bar{i}_b$, $\bar{v}_1$, $\bar{v}_2$, and $\bar{v}_C$, are the state values in the operation point and $\tilde{x}$ represents the deviation of the variable x.

Proportional–Integral control design to currents

In the linearized system (2.16), neglecting the parallel resistance of the supercapacitors (R_C) of (2.14) and (2.15) due to its high value, and considering the capacitance is enough to kept the voltages constant during operation of the system, it is assumed that the dynamic of the currents are governed by a first–order system. Therefore, the current equations are,

$$\begin{aligned} \tilde{\bar{i}}_1 &= \frac{\tilde{u}_1 \bar{v}_C}{sL_1 + R_1}, \\ \tilde{\bar{i}}_2 &= \frac{\tilde{u}_2 \bar{v}_C}{sL_2 + R_2}, \\ \tilde{\bar{i}}_3 &= \frac{\tilde{u}_3 \bar{v}_C}{sL_3 + R_3}. \end{aligned} \tag{2.21}$$

Hence, PI controllers of the form $k_j(sT_j+1)/sT_j$ can provide an appropriate performance in close-loop, thus the resulting close-loop dynamics are

$$\begin{aligned}
\frac{\tilde{i}_1}{\tilde{i}_1^*} &= \frac{k_1\bar{v}_C}{T_1L_1} \quad \frac{sT_1+1}{s^2+s(\frac{R_1+k_1\bar{v}_C}{L_1})+\frac{k_1\bar{v}_C}{T_1L_1}},\\
\frac{\tilde{i}_2}{\tilde{i}_2^*} &= \frac{k_2\bar{v}_C}{T_2L_2} \quad \frac{sT_2+1}{s^2+s(\frac{R_2+k_2\bar{v}_C}{L_2})+\frac{k_2\bar{v}_C}{T_2L_2}},\\
\frac{\tilde{i}_3}{\tilde{i}_3^*} &= \frac{k_3\bar{v}_C}{T_3L_3} \quad \frac{sT_3+1}{s^2+s(\frac{R_3+k_3\bar{v}_C}{L_3})+\frac{k_3\bar{v}_C}{T_3L_3}}.
\end{aligned} \tag{2.22}$$

As can be seen from (2.22), the dynamics in close-loop of the currents can be approximated by a second order system, in which case the damping ratio is identified as

$$\begin{aligned}
\xi_1 &= \frac{R_1+k_1\bar{v}_C}{2L_1\omega_1},\\
\xi_2 &= \frac{R_2+k_2\bar{v}_C}{2L_2\omega_2},\\
\xi_3 &= \frac{R_3+k_3\bar{v}_C}{2L_3\omega_3}.
\end{aligned} \tag{2.23}$$

Moreover, we can identify the oscillation frequency of the current close–loop controller as

$$\omega_1=\sqrt{\frac{k_1\bar{v}_C}{T_{i_1}L_1}}, \quad \omega_2=\sqrt{\frac{k_2\bar{v}_C}{T_2L_2}}, \quad \textit{and} \quad \omega_3=\sqrt{\frac{k_3\bar{v}_C}{T_3L_3}}. \tag{2.24}$$

Choosing the settling time for the currents of the system ($T_j,\ j=1,2,3$) and a proper damping ratio ($\xi_j,\ j=1,2,3$) in order to limit the overshoot, from (2.23) and (2.24) we calculate the constants of the PI controllers T_j and k_j (see appendix B.1 for details). Since the system is composed of pulse wide modulated (PWM) dc converters with a switching frequency equal to 20 kHz (carrier frequency f) and the control signals must respond slower than this frequency in order to ensure the correct operation, the settling time chosen is 10 times $1/f$ ($T_j=10/f$). To guaranty a fast dynamic response with 10% maximum overshoot, the value of the damping ratio must be in the range $0.6<\xi_j<1$, in this work the chosen value was $\xi_j=0.707$.

Proportional–Integral control design to the DC–link voltage

Since the battery is in charge of controlling the voltage of the DC–link voltage (v_C), a proportional plus integral (PI) controller is designed to drive the v_C error to zero, the output of this controller is the battery current reference (i_3^*). To uncouple the voltage controller from the current controller and to avoid internal resonance, the time response is set to 10 times slower than the current controller, so the settling time of the voltage controller is $T_4=100/f$. With this time separation, it can be assumed that $\tilde{i}_3=\tilde{i}_3^*$ and

that $\tilde{u}_1, \tilde{u}_2$ and $\tilde{u}_3$ are approximately 0. Therefore, from the linearized system (2.17), it the dynamic of the voltage v_C in terms of the current i_3^* is obtained,

$$\tilde{v}_C = \frac{\tilde{i}_3^* \bar{u}_3}{sC_C}. \tag{2.25}$$

The dynamics corresponds to a first–order system, so a linear controller of the form $k_4(sT_4+1)/sT_4$ can provide good performance in a close–loop. Thus close–loop dynamics is

$$\frac{\tilde{v}_C}{\tilde{v}_C^*} = \frac{k_4\bar{u}_3}{T_4C_C} \quad \frac{sT_4+1}{-s^2+s(\frac{k_4\bar{u}_3}{C_C})+\frac{k_4\bar{u}_3}{T_4C_C}}. \tag{2.26}$$

As can be seen in (2.26), the close-loop dynamics has the form of a second–order system therefore, we can identify the damping ratio (ξ_4) and the oscillation frequency (ω_4) of the close-loop as

$$\xi_4 = \frac{k_4\bar{u}_3}{2C_C\omega_4}, \tag{2.27}$$

$$\omega_4 = \sqrt{\frac{k_4\bar{u}_3}{T_4C_C}}. \tag{2.28}$$

Following the same design criteria of the current controllers, to establish a time separation between the two control loops, a settling time (T_4)that is 10 times faster than the settling time of the current controller is chosen. Moreover, to ensure a fast response and limit the overshoot to 10%, a value $\xi_4 = 0.707$ is chosen.

2.3.2 Current reference selection

The system is operated by keeping the multiport voltages bounded away from zero. Consequently, the current references are selected according to the simple formula (2.7) that, in the present scalar case, reduces to

$$i_j^\star(t) = F_j(v_j(t)) = \frac{P_j^\star(t)}{v_j(t)}, \quad j = 1, 2, 3. \tag{2.29}$$

To illustrate the capabilities of the new DER to transfer the energy between the multiports, we considered the same energy management scenario of the previous section, but with the following essential modifications.

– During certain periods of time the energy of one supercapacitor is transferred to the other–with the profiles and magnitudes specified before–while the battery provides the energy dissipated in the DER. That is, we select $P_1^\star(t) = -P_2^\star(t), \quad P_3^\star(t) = d_I(t)$.

– During the whole simulation horizon $P_3^\star(t)$ is determined–according to the expression above–from the measured losses in the DER, which are given by

$$d_I(t) = R_1 i_1^2(t) + R_2 i_2^2(t) + R_3 i_3^2(t).$$

A profile of the function $P_1^\star(t)$ that implements this strategy–that obviously mimics $\alpha(t)$–is shown in Fig. 2.4. The remaining task is the design of a control strategy for the system (2.8)–(2.11), (2.14), and (2.15), which ensures the tracking of the current references defined in (2.29). Notice that the only parameters needed for the definition of the current references are the DER resistors R_j, which are reasonably well known.

2.4 Simulation and Experimental Results of the new DER

In this section, the new DER proposed in subsection 2.2.3 is tried in experiments. To compensate for the losses in the DER, we added a third multiport that consists of a simple battery, whose control is fixed by the energy management policy described in subsection 2.2.4.

2.4.1 Proportional–Integral control to the new DER

In this case, each converter switch is regulated via a PI controller, which is formulated in a compact form by

$$u_j(t) = -k_{pj}\tilde{i}_j(t) - k_{ij}\int_0^t \tilde{i}_j(s)ds, \quad j = 1, 2, 3, \tag{2.30}$$

where $k_{pj}, k_{ij} > 0$ are the proportional and integral gains, respectively. The controllers gains are selected using the standard linear control techniques described subsection 2.3.1 and in [25], [26], [27] based on the linearization of the system around an operation point and trying to enforce a time–scale separation between the loops, and are summarized in appendix B.1.

Simulation results of the new DER

Simulations of the system (2.8)-(2.11), (2.14), and (2.15) with the PI controllers, were done in Simulink and the results are shown in Figs. 2.8, 2.9, and 2.10. It is clear from Fig. 2.8 (b) that the desired energy transfer, that is, tracking of the signal $P_1^\star(t)$, is carried out almost perfectly in Fig. 2.8 (a).

This is due to the fact that, as shown in Fig. 2.9 (b), the tracking error in the multiport currents is negligible, even during the transient. As predicted by the theory, with the new strategy, the injection of the current in Fig. 2.9 (a) from the battery that compensates the losses in the DER, drives the power of the DER to zero.

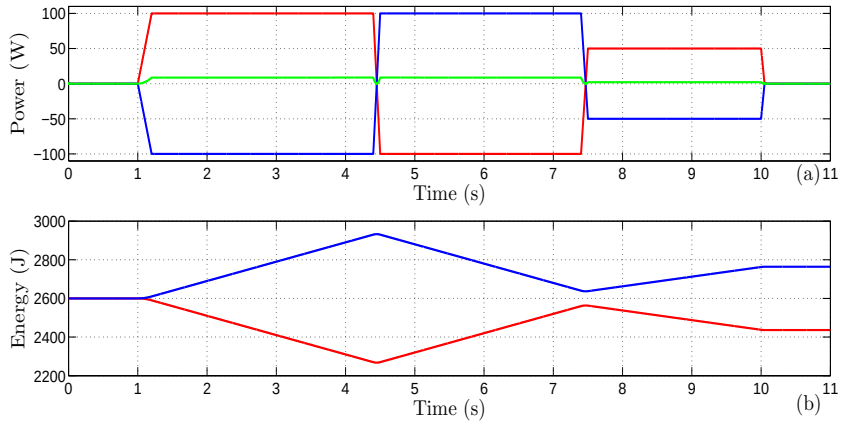

Figure 2.8: Simulation results for the PI control (2.30): a) Power curves of the DER $\dot{H}_1(t)$ and $\dot{H}_2(t)$ in red and blue, respectively, and $d_I(t)$ in green. b) Evolution of the energy stored as $H_1(t)$) and $H_2(t)$ in red and blue, respectively.

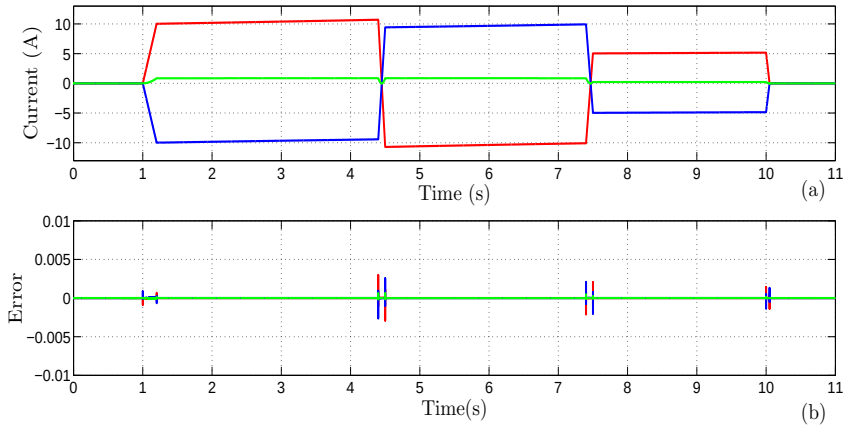

Figure 2.9: Simulation results for the PI control (2.30): a) Currents of the DER i_1 and i_2 in red and blue, respectively, and i_3 in green. b) Errors of the DER $\tilde{i}_1(t)$, $\tilde{i}_2(t)$ in red and blue, respectively and $\tilde{i}_3(t)$ in green.

Experimental results of the new DER

Using the same test bench from Fig. 2.6, experiments were carried out and the results are shown in Figs. 2.11, 2.12 and 2.13.

As seen in the figures, the desired power transfer between the supercapacitors is ensured. In Fig. 2.11, the power exchanged between the supercapacitors follows the same $P_1^\star(t)$ and $P_2^\star(t)$ pattern of the experimental results, yet there is no degradation of the power functions $P_1(t)$ and $P_2(t)$, while the battery transfers the power $d_I(t)$ required to compensate for the DER losses and the DC link voltage.

It is observed in Fig. 2.12 that the current tracking errors are larger than the ones obtained for the DS–DER (see Fig. 1.17.). The DC link voltage in Fig. 2.13 starts

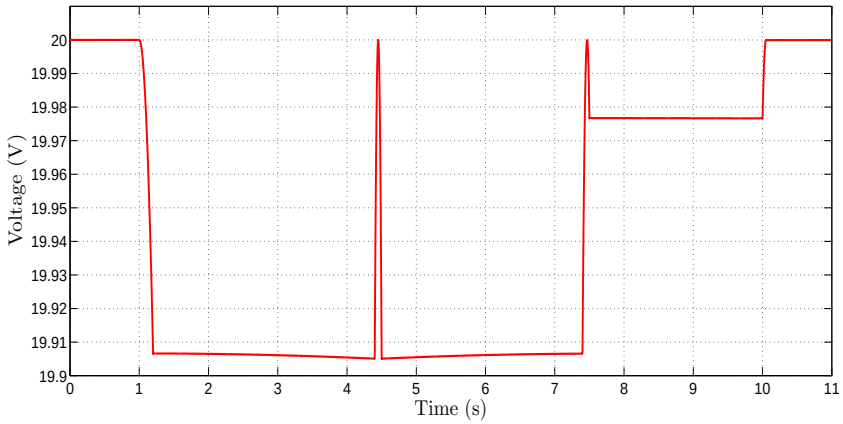

Figure 2.10: Simulation results for the PI control (2.30): DC link voltage $v_C(t)$.

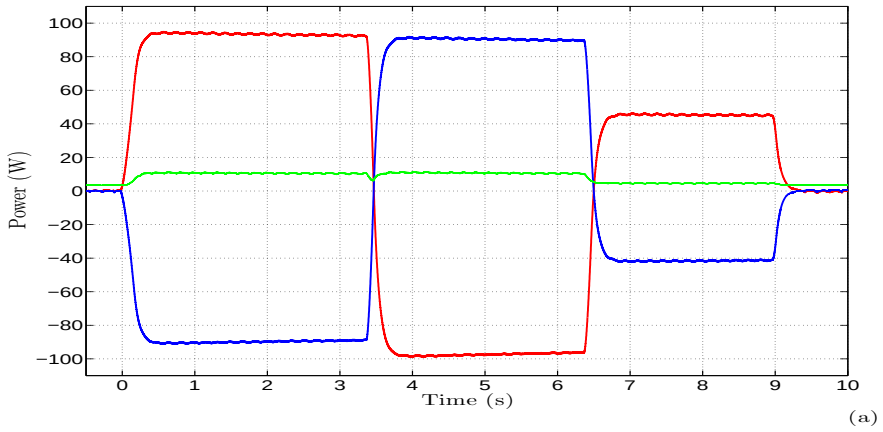

Figure 2.11: Experimental results for the PI control (2.30): a) Power in ports Σ_1, Σ_2, and Σ_3, power $\dot{H}_1(t)$ and $\dot{H}_2(t)$ in red and blue, respectively, and $d_I(t)$ in green.

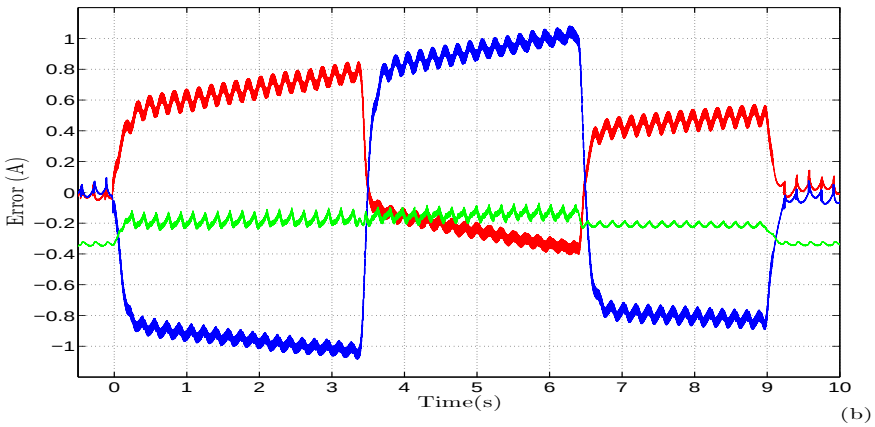

Figure 2.12: Experimental result for the PI control (2.30): b) Errors $\tilde{i}_1(t)$, $\tilde{i}_2(t)$, $\tilde{i}_3(t)$, in red, blue, and green, respectively.

the experiment with 20.5 V as the initial condition in a stationary state, after 0 s when controllers are working, the average variation is less than 1 V to keep the DC–link voltage within reasonable values.

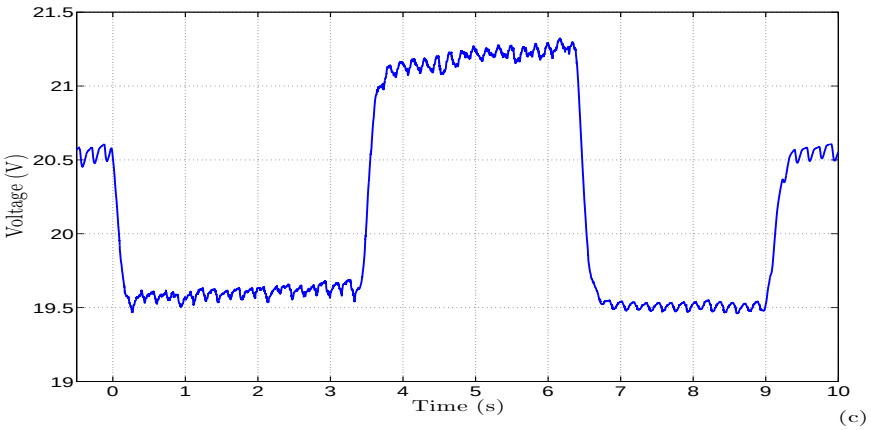

Figure 2.13: Experimental result for the PI control (2.30): c) DC link-voltage capacitor (v_C).

2.4.2 An approximate input–output linearizing controller

In spite of the good performance achieved by the PI control, for the sake of completeness, an approximate input–output feedback linearization controller for the DER was also tested. This is given by the follow compact form,

$$\begin{aligned} u_j(t) &= \frac{1}{v_C(t)}[v_j(t) - R_j i_j(t) - L_j \frac{di_j^\star}{dt}(t)] + \\ &\quad + \frac{\gamma_j}{v_C(t)}[L_j \tilde{i}_j(t)], \; j = 1, 2, 3, \end{aligned} \tag{2.31}$$

where $\gamma_j > 0$ are tuning parameters. Indeed, replacing 2.31 in (2.8)-(2.11), (2.14), and (2.15)) yields the simple linear and exponentially stable system

$$\frac{d\tilde{i}_j}{dt}(t) = -\gamma_j \tilde{i}_j(t), \quad j = 1, 2, 3,$$

which implies that the current–tracking errors converge to zero exponentially fast, at a rate determined by γ_j, achieving the desired objective.

The only parameters needed for the implementation of (2.31) are R_j and L_j, which are in the DER, hence are reasonably well known. On the other hand, the control requires the term $\frac{di_j^\star}{dt}(t)$. Recalling that $i_j^\star(t)$ is defined by (2.29), it is clear that to compute its derivative, the dynamics of the multiports, *ie* (2.8)-(2.11), (2.14), and (2.15), must be taken into account. Besides the fact that the resulting control law becomes extremely

involved, the multiport dynamics are highly uncertain in a practical scenario. Therefore, we propose to obtain $\frac{di_j^\star}{dt}(t)$ with an approximate differentiation filter

$$W(s) = \frac{bs}{\tau s + 1}.$$

The controller parameters used in the simulations were $\gamma_1 = \gamma_2 = \gamma_3 = 1000$, $b = 1$, and $\tau = 0.00003$.

Experimental results of the new DER

The behavior of the new controller observed in the simulations was almost identical to the PI scheme of the previous section therefore, the plots are omitted to pass directly to the experimental curves.

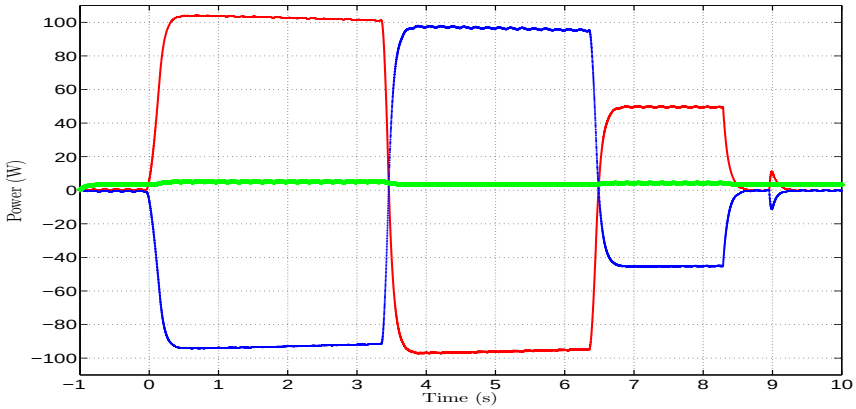

Figure 2.14: Experimental results for the input–output linearizing control (2.31): Power in ports Σ_1, Σ_2, and Σ_3, power $\dot{H}_1(t)$ and $\dot{H}_2(t)$ in red and blue, respectively, and $d_I(t)$ in green.

There are certain differences that were observed in the behavior of the DC–link voltage using the same test bench as Fig. 2.6, the desired power transfer between the supercapacitors is ensured. In Fig. 2.14, the power exchanged between the supercapacitors follows the same $P_1^\star(t)$ and $P_2^\star(t)$ pattern of the previous experiments, yet there is no degradation of the power function of $P_1(t)$ and $P_2(t)$. The battery transfers the power $d_I(t)$ required to compensate for the DER losses and the DC–link voltage. We observed small deviation with respect to the initial condition, the stationary state is reached after 0.5 s in 20.5 V as in the previous experiments, however the variation of DC–link voltage is greater than previous controls due to the differential term in (2.31), this feature is of paramount importance in applications where capacitors with a small capacity are used in the DC–link voltage and may justify the use of the, admittedly more complex, linearizing control strategy.

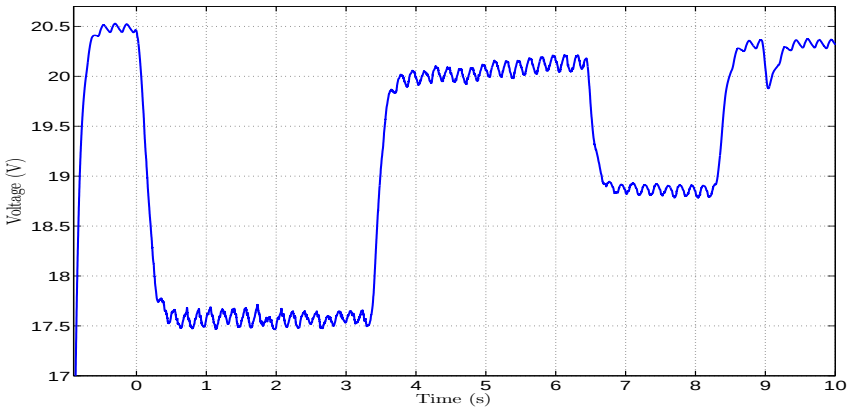

Figure 2.15: Experimental result for the input–output linearizing control (2.31): DC link-voltage capacitor (v_C).

2.5 *Ad–hoc* Modifications to the DS–DER

Although the new DER showed remarkable performance that can be theoretically justified, it requires the knowledge of the losses in the DER, which are difficult to model in a switching device. For this reason, it is interesting to try other practically motivated options to render the original DS–DER operative. A first attempt was the standard solution of nested PI loops to drive the DC voltage error to zero

$$\widetilde{v}_C(t) := v_C(t) - v_C^\star.$$

That is, the inputs (1.22) are replaced by

$$\begin{aligned} w_j(t) &= -k_{p_j}\widetilde{i}_j(t) - k_{i_j}\int_0^t \widetilde{i}_j(s)ds - \\ &- k_{pv}\widetilde{v}_C(t) - k_{iv}\int_0^t \widetilde{v}_C(s)ds,\ j = 1, 2, \end{aligned} \tag{2.32}$$

where we notice the addition of an outer–loop PI in the voltage errors. This new controller was experimentally tested showing a marginal improvement with respect to the control (1.22), in the sense that the decrease of the DC–link voltage to zero took a long time. Clearly, this phenomenon is unavoidable without the inclusion of additional energy to compensate for the losses in the DER.

A second alternative is to add an external regulated battery, as done in the new DER, but not to treat it as an additional multiport. Instead, the battery is regulated via nested

current and voltage PIs—a configuration that is standard in applications. That is,

$$\begin{aligned} i_b^\star(t) &= -k_{pv}\widetilde{v}_C(t) - k_{iv}\int_0^t \widetilde{v}_C(s)ds \\ \tilde{i}_b(t) &= i_b(t) - i_b^\star(t) \\ u_3(t) &= -k_{pb}(\widetilde{i}_b(t)) - k_{ib}\int_0^t (\widetilde{i}_b(s))ds. \end{aligned} \tag{2.33}$$

Moreover, we propose to add to the reference signals generated by the DS–DER the reference signal $i_b^\star(t)$ weighted by a switch that decides the direction of the flow of the battery current as a function of the sign of the parameter $\alpha(t)$—we refer to it as a directional DER in the sequel to this scheme. This leads to the following new definition of the supercapacitors currents references

$$\begin{aligned} i_1^\star(t) &= \alpha(t)v_1(t)v_2^2(t) \; - \frac{[1-\text{sign}(\alpha(t))]\, i_b^\star(t)}{2} \\ i_2^\star(t) &= -\alpha(t)v_1^2(t)v_2(t) \; - \frac{[1+\text{sign}(\alpha(t))]\, i_b^\star(t)}{2}. \end{aligned} \tag{2.34}$$

2.5.1 Experimental results of the directional DER

The directional DER was implemented with linear PI controllers for the two multiports, that is

$$u_j(t) = -k_{p_j}\tilde{i}_j(t) - k_{i_j}\int_0^t \tilde{i}_j(s)ds, \; j = 1, 2. \tag{2.35}$$

Controller gains that are used for the experiments are $k_{p1} = k_{p2} = 0.2151$, $k_{i1} = k_{i2} = 0.0012$, $k_{pb} = 0.2511$, $k_{ib} = 0.001$, $k_{pv} = 0.2133$, and $k_{iv} = 0.00127$. Experimental results are shown in Figs. 2.16, 2.17, and 2.18. The experimental behavior of the directional DER was good because the desired power transfer between ports was ensured. The power exchanged between the supercapacitors follows the same $i_1^\star(t)$ and $i_2^\star(t)$ pattern as in the previous experiments, see Fig. 2.16. The battery compensates for the losses indirectly by regulating the DC–link voltage with another PI (2.33).

The current tracking errors are considerably small. In the DC–link voltage curve, a short deviation was observed with respect to the initial condition, and in this case reached 19.5 V. The variation of the DC–link voltage is good with this controller, which unfortunately, cannot be theoretically analyzed.

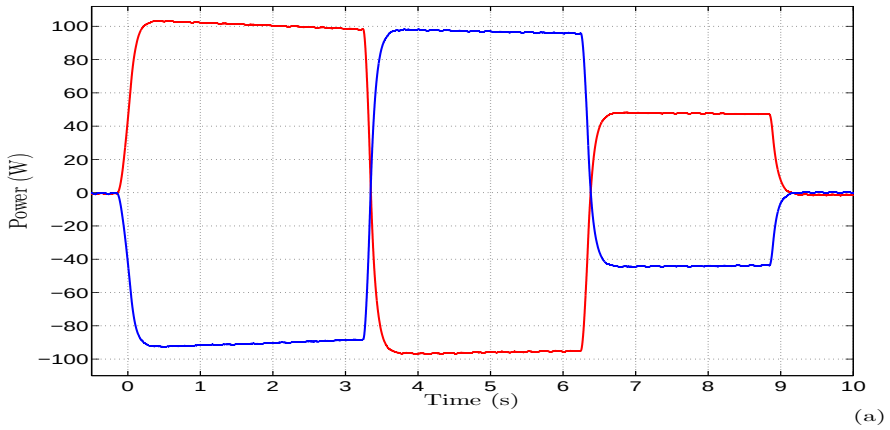

Figure 2.16: Experimental results of the directional DER, PI control (2.33)–(2.35): a) Power in the ports Σ_1 and Σ_2, $P_1(t)$ in red, $P_2(t)$ in blue.

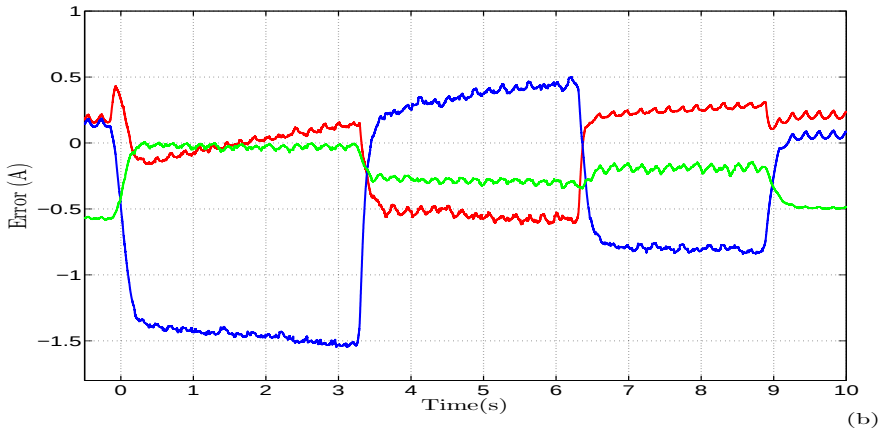

Figure 2.17: Experimental results of the directional DER, PI control (2.33)–(2.35): b) Errors $\tilde{i}_1(t)$, $\tilde{i}_2(t)$, $\tilde{i}_3(t)$, in red, blue, and green, respectively.

2.6 Conclusions

Limitation of the DS–DER was reported in the previous chapter emphasizing the behavior after a long energy transfer time where in a lossless systems the energy is conserved. Namely, due to the power–preserving nature of the DS–DER, the energy of the interconnection system–that is implemented with power electronic devices–decreases asymptotically in the presence of dissipation, rendering the DS–DER asymptotically dysfunctional, see (2.2). Two ad–hoc modifications to overcome this fundamental shortcoming were proposed and tested in a experimental test bench: (i) adding an outer–loop PI regulator for the DC–link voltage; and (ii) providing energy to the DER with an external source. The first alternative turned out to be inadequate, both from the perspectives energy management and voltage regulation. On the other hand, adding an external battery effectively

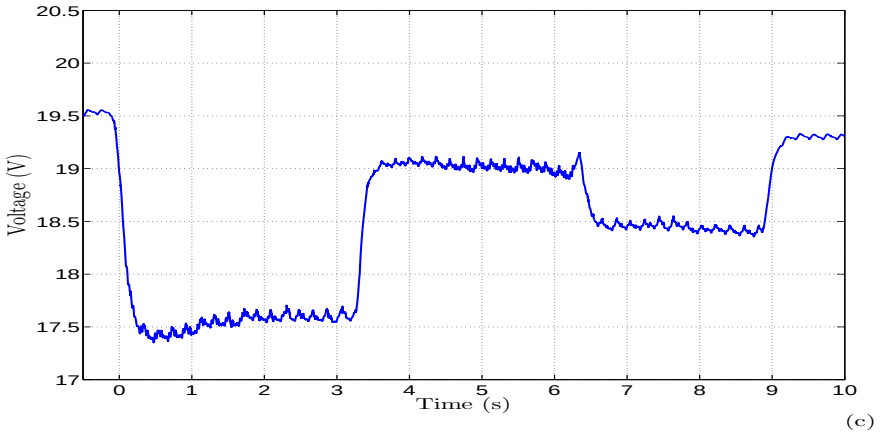

Figure 2.18: Experimental results of the directional DER, PI control (2.33)–(2.35): c) DC link-voltage capacitor (v_C).

removed the problem, but does not seem to be a practically reasonable solution. It is important to overscore that the energy of the interconnection system will always decrease in the DS–DER, hence a malfunction is still present even if we treat the battery as a third port—as done with the new DER.

Instead, it was proposed to lose the power–preserving feature of the DS–DER, and a new DER, that takes into account the losses, was proposed. The new DER was tested in simulations and experiments using a simple PI scheme and an (approximate) input–output linearizing controller. The performance in both cases was excellent with the latter controller achieving, at the prize of higher complexity, a better regulation of the DC link voltage. Besides the new DER, an (ad–hoc) outer–loop switched PI controller, called a directional DER, was proposed and tested in simulations and experiments revealing excellent performance and ease of tuning.

The application of these ideas are currently being investigated for a realistic fuel–cell based system. Toward this end, novel multiport converter topologies are being explored to solve the same problems, see [29].

On the theoretical side, a question that remains to be addressed is the robustness of the new DER, in particular, *vis–à–vis* parameter uncertainty. As shown in the experiments in subsection 2.2.3, the actual dissipation–whose value is needed to define the references–may significantly differ from the one predicted by the lumped parameter model. Hence, to enhance its robustness, an adaptive version of the DER must be worked out. Another interesting, though hard, theoretical question involves a stability analysis of the directional DER. Invoking time–scale separation arguments, this analysis seems feasible. However, this is not the scenario that was observed in our experimentation where, to obtain a good performance, both loops must operate at the same time–scale.

Chapter 3

Globally Convergent Estimator of Pressure in a FC System

3.1 Introduction

Electrical energy generation by means of clean energy sources are an interesting current issue to actual research. Owing that they represent an alternative energy in contrast with non renewable energies, their ecological advantages in the electricity production have contributed to the reduction in the air pollution, global warming, and others, several affectations around the world caused by combustion of non renewable fuels (petroleum, coal, etc.).

The proton–exchange membrane (PEM) fuel cells are part of this clean energy source group. These electromechanical-chemical devices generate electricity through a chemical process between a group of gases (hydrogen, oxygen) and a catalyst. In a particular case, this energy supply is planning to be implemented in transports that are based on interconnection sources and load systems, previously observed in Chapter 1 and Chapter 2 of this thesis work. The basis of the physical phenomenon principle of PEM fuel cells (FC) exposed in [44] and [45] give us fundamental physical laws to formulate the nonlinear FC model in [43]. To analyze this dynamic, the FC model is normally divided into two subsystems. The first subsystem is the compressor composed by motion mechanical parts, the second is the group of cells integrated by static mechanical elements, both are modeled by a group of differential equation, see [42].

The electrical output behavior of FC is commonly represented by a voltage-current polarization curve. This is the mathematical relationship of functions that depends on fiscal variables and parameters of mechanical-electrical-chemical design evolving over time. To analyzer FC dynamic model, it is necessary to know certain physical variables such as: humidity, temperature, pressure, voltage, and current. This set of variables usually measure by electrical-electronic sensors permit an evaluation of the data through the

computer to some specific purpose such as to know that the FC is working with in the correct physical limits, to prevent damage and aging in the PEMFC system, to analyze and validate the mathematical dynamic model *vs* real, and to design the nonlinear control of the plant with feedback loops for the measurements. However, all the FC variables are not convenient to measure. The input gas (hydrogen and oxygen) pressure present in a PEMFC is one, because this measurement device is expensive, it needs frequent maintenance, useful life is short, the distribution, calibration, and adaptation of small plants are limited and the display value is not correct. To solve this problem, one design of a global convergent estimator (GCE) in [35], [36] on this application is proposed using the principles of immersion and invariance theory recently reported in a control literature, see [37]-[41].

The Lyapunov's second stability theorem is called upon to solve stability problems of FC behavior functions that is strictly monotonically increasing.

In the case of hydrogen gas pressure, it does not concern our problem because it is supplied by tanks. It means having constant value of pressure for this specific gas. On the other hand, the oxygen gas pressure is taken from the environment through an air compressor. This electrical machine is responsible for the increase or decrease in the pressure of oxygen in the PEMFC pipes.

The chapter is organized in a follow form. In section 3.2, the formulation of a globally convergent estimator is given. The PEM fuel cell voltage-current behavior is exposed in section 3.3. While in section 3.4, the oxygen pressure estimator in a PEM fuel cell system is presented. In section 3.5, the simulation results are showed and the chapter ends with some concluding remarks in section 3.6.

3.2 Formulation of Globally Convergent Estimator

In this section, the design of a globally convergent estimator (GCE) is formulated assuming we have a function F in 3.1 that represent the system behavior of our plant. In this function, it is possible to distinguish two kinds of terms, they are measurable and not measurable, see [39], these terms basically depend of two variables θ and ξ that are expressed as follow,

$$F = G(\theta) + H(\xi) + K(\theta, \xi), \tag{3.1}$$

where $\theta > 0$ and $\xi > 0$ and where ξ is known and depends on time θ, such that the measurable signals F and $H(\xi)$ are represented by,

$$y(t) = F + H(\xi). \tag{3.2}$$

Indeed, the representation in nonlinear regression form will be

$$y(t) = \phi(\theta, \xi), \tag{3.3}$$

where

$$\phi(\theta, \xi) := G(\theta) + K(\theta, \xi). \tag{3.4}$$

After this formulation, the follow proposition is presented:

Proposition 3.1. *: Consider the function $\phi(\theta, \xi)$, where F and $H(\xi)$ are known and corresponds to a nonlinear regression model. The convergent estimator is*

$$\dot{\hat{\theta}} = \gamma(y - \phi(\hat{\theta}, \xi)) \tag{3.5}$$

with $\gamma > 0$, which ensure that:

$$\lim_{t\to\infty} \hat{\theta} = \theta. \tag{3.6}$$

For all initial conditions $\hat{\theta}(0)$ and all positive measurable signals $H(\xi)$, F.

Proof. : For estimator to converge to a desired value, it is necessary to exploit the monotonicity of map $\theta \mapsto \phi(\theta, \xi)$

$$\frac{\partial \phi(\theta, \xi)}{\partial \theta} > 0, \tag{3.7}$$

which is defined as positive. Hence, the function is strictly monotonically increasing and satisfies

$$(\hat{\theta} - \theta)\left[\phi(\hat{\theta}, \xi) - \phi(\theta, \xi)\right] > 0, \quad \forall \hat{\theta} \neq \theta. \tag{3.8}$$

Take the Lyapunov function as a candidate,

$$V(\hat{\theta}) = \frac{1}{2\gamma}(\hat{\theta} - \theta)^2. \tag{3.9}$$

Its derivative, along the trajectories of (3.2), (3.3), (3.4), and (3.5) is given by

$$\dot{V} = -(\hat{\theta} - \theta)[\phi(\hat{\theta}, \xi) - \phi(\theta, \xi)] < 0, \quad \forall \hat{\theta} \neq \theta. \tag{3.10}$$

Therefore, the bound follows immediately from (3.8). Accordingly $V(\hat{\theta})$ is a *strict Lyapunov function* and the proof is completed calling upon Lyapunov's second stability theorem. □□□

3.3 Fuel Cell Voltage-Current Behavior

An useful mathematical equation to represent PEM fuel cell voltage by cell V_c is expressed by four essential functions of voltage. First, Nernst tension, which represents the voltage supply $E_{th}(\theta)$ and second, all of the electrical losses involved in the nonlinear system. This group of functions includes activation, ohmic, and concentration losses.

$$V_c = E_{th}(\theta) - V_{ohm}(\xi) - V_{act}(\theta, \xi) - V_{con}(\theta, \xi). \tag{3.11}$$

E_{th} is Nernst tension produced by the chemical reaction of FC. V_{act}, V_{ohm}, and V_{con} are losses by activation, electrical resistance, and concentration. These functions depend on θ, which represents oxygen pressure and ξ, which is the current of the PEM fuel cell, so that each function of voltage is expressed in follow form:

* *Open loop voltage* in the FC, called the tension of *Nernst*, is the maximum work obtained from one cell that corresponds to a Gibbs Free Energy exchange as a result of the difference between reactants product and Gibbs free energy. It is formulated as follows,

$$E_{th}(\theta) = d_1 + d_2 \ln\left(\frac{\theta + \rho_{h_2}}{p_{atm}}\right) + \frac{1}{2} \ln\left(\frac{\theta}{p_{atm}}\right), \tag{3.12}$$

  where ρ_{h_2} is a constant positive and represents the hydrogen pressure. T_{st} is the stack temperature and T_{atm} is the atmospheric temperature, both are constants using the Kelvin as a unit where $T_{st} \in \mathbb{R}_+, T_{atm} \in \mathbb{R}_+$.

* *Ohmic voltage drop* is produced by the ohmic resistance of a PEMFC that consists of the electrical resistance of a polymer membrane, electrical resistance between the membrane and electrodes, and the electrical resistances of electrodes. The overall ohmic voltage drop can be expressed as

$$V_{ohm}(\xi) = \frac{\xi\, R_{ohm}}{A_{fc}}, \tag{3.13}$$

  where $R_{ohm} > 0$ is the electrical resistance of the surface per cell.

* *Activation voltage drop* is knowing the Tafel equation, given below, which is used to calculate the activation voltage drop in a PEMFC.

$$V_{act}(\theta) = V_o + \frac{1}{2} V_a (1 - e^{-c_4 \frac{\xi}{A_{fc}}}) \tag{3.14}$$

$$V_o = d_3 + d_2 \ln\left(\frac{\theta + \rho_{h_2}}{p_{atm}}\right) + \frac{1}{2} \ln\left(\frac{0.1173(\theta + \rho_{h_2})}{p_{atm}}\right) \tag{3.15}$$

$$V_a = d_4 \left(\frac{\theta}{0.1173} + \rho_{h_2} \right)^2 + d_5 \left(\frac{\theta}{0.1173} + \rho_{h_2} \right) + d_6, \tag{3.16}$$

where $C_1 \in \mathbb{R}_+$ is a constant and $p_{sat} \in \mathbb{R}_+$ is the saturation pressure in pascal units.

* *Concentration voltage drop* is generated during the reaction process, concentration gradients can be formed due to mass diffusions from the flow channels to the reaction sites (catalyst surfaces). At high current densities, slow transportation of reactants (products) to (from) the reaction sites is the main reason for the concentration voltage drop. Any water film covering the catalyst surfaces at the anode and cathode can be another contributor to this voltage drop. The concentration overpotential in the fuel cell is defined as

$$V_{con}(\theta, \xi) = \xi {A_{fc}}^{-1} \left(C_2 \xi {A_{fc}}^{-1} {Imax}^{-1} \right)^{C_3} \tag{3.17}$$

$$C_2 = c_{15}\ \Psi^{'}\ (c_{14}\,\theta + p_{sat}) + \Upsilon^{'}, \tag{3.18}$$

where c_{14} and c_{15} are positive constants, see values in appendix C.1, $\Psi^{'}$ and $\Upsilon^{'}$ are noncontinuous functions depending on θ, they are bounded as follows,

$$\Psi^{'} := \begin{cases} A_1 & \lambda(\theta) < 0 \\ A_2 & 0 \leq \lambda(\theta) \end{cases} \tag{3.19}$$

$$\Upsilon^{'} := \begin{cases} B_1 & \lambda(\theta) < 0 \\ B_2 & 0 \leq \lambda(\theta) \end{cases}. \tag{3.20}$$

Constants A_1, A_2, B_1, and B_2 are positives, they depend on the stack temperature, see values in appendix C.2. The function $\lambda(\theta)$ in appendix C.3 is a relationship between oxygen pressure θ, atmospheric pressure p_{atm}, and saturation pressure vapor p_{sat}, see appendix C.3.

Lemma 3.1. *Functions $\Psi^{'}$ and $\Upsilon^{'}$ are discontinuous, therefore, approximating them in a continuous form, we have $\Psi^{'} \cong \Psi$ and $\Upsilon^{'} \cong \Upsilon$ where,*

$$\Psi = 1/2\, A_1 + 1/2\, A_2 + 1/2\ (A_1 - A_2) \tanh\left(\lambda(\theta)\right) \tag{3.21}$$

$$\Upsilon = 1/2\, B_1 + 1/2\, B_2 + 1/2\ (B_1 - B_2) \tanh\left(\lambda(\theta)\right), \tag{3.22}$$

where $C_3 \in \mathbb{R}_+$ is a constant.

The value of the constants like temperature, pressure, and other physical parameters implemented in E_{th}, V_{act}, V_{ohm}, and V_{con} functions are showed in appendix C.3.

3.4 Estimator of Oxygen Pressure for a Fuel Cell

In this section, the example of the compact form in (3.2) is used; measurable signals for the equation (3.11) are defined as follow

$$y(t) = V_c + V_{ohm}(\xi). \tag{3.23}$$

Indeed, the representation in a nonlinear regression form will be

$$y(t) = \phi(\theta, \xi). \tag{3.24}$$

Where,

$$\phi(\theta, \xi) := E_{th}(\theta) - V_{act}(\theta, \xi) - V_{con}(\theta, \xi). \tag{3.25}$$

After this formulation, the proposition for the fuel cell system is presented.

Proposition 3.2. *: Consider the function $\phi(\theta, \xi)$, where V_c and $V_{ohm}(\xi)$ are known and correspond to a nonlinear regression model. The gradient estimator of oxygen pressure (OP) is*

$$\dot{\hat{\theta}} = \gamma(y - \phi(\hat{\theta}, \xi)), \tag{3.26}$$

with $\gamma > 0$ to ensure that:

$$\lim_{t \to \infty} \hat{\theta} = \theta. \tag{3.27}$$

For all initial conditions $\hat{\theta}(0)$, $\theta : \mathbb{R}_+ \to \mathbb{R}_+$ and $\xi : \mathbb{R}_+ \to \mathbb{R}_+$, and all positive measurable signals V_c and $V_{ohm}(\xi)$ are defined as positive.

Proof. : for the estimator the converge to the desired value, it is necessary to exploit the monotonicity of the map $\theta \mapsto \phi(\theta, \xi)$:

$$\frac{\partial \phi(\theta, \xi)}{\partial \theta} = \frac{1}{2\theta} - \frac{c_1}{(\theta + \rho_{h_2})} + (c_2\,\theta + c_3)\left(1 - \mathrm{e}^{-\frac{\xi}{c_4}}\right) - \frac{\xi^3 \vartheta \varpi}{c_5} \tag{3.28}$$

$$\vartheta = \left(\left(c_6 - c_7\,(\varphi)^2\right)(c_8\,\theta + c_9)\, + c_{10} + c_{11}\,\varphi\right) \tag{3.29}$$

$$\varpi = \left(\left(c_7 - c_7\,(\varphi)^2\right)(c_8\,\theta + c_9)\, + c_{11} + c_{12}\,\varphi - c_{11}\,(\varphi)^2\right) \tag{3.30}$$

$$\varphi = \tanh\left(\theta - c_{13}\right). \tag{3.31}$$

The function $\phi(\theta, \xi)$ is strictly monotonically increasing, if and only if, it satisfies, $\xi \geq 0$ and $\theta > c_{13}$

$$\left(c_2\,\theta + c_3\right)\left(1 - \mathrm{e}^{-\frac{\xi}{c_4}}\right) \geq 0 \tag{3.32}$$

$$\frac{\xi^3 \vartheta \varpi}{c_5} + \frac{c_1}{(\theta + \rho_{h_2})} < \frac{1}{2\theta} + \left(c_2\,\theta + c_3\right)\left(1 - \mathrm{e}^{-\frac{\xi}{c_4}}\right), \tag{3.33}$$

which is defined as positive and satisfies:

$$(\hat{\theta} - \theta)\left[\phi(\hat{\theta}, \xi) - \phi(\theta, \xi)\right] > 0, \quad \forall \hat{\theta} \neq \theta. \tag{3.34}$$

Take the Lyapunov function as a candidate,

$$V(\hat{\theta}) = \frac{1}{2\gamma}(\hat{\theta} - \theta)^2. \tag{3.35}$$

Its derivative, along the trajectories of (3.23), (3.24), (3.25), and (3.26) is given by

$$\dot{V} = -(\hat{\theta} - \theta)[\phi(\hat{\theta}, \xi) - \phi(\theta, \xi)] < 0, \quad \forall \hat{\theta} \neq \theta. \tag{3.36}$$

Therefore, the bound follow immediately from (3.34). Accordingly, $V(\hat{\theta})$ is a *stric Lyapunov function* and the proof is completed calling upon Lyapunov's second stability theorem. □□□

3.5 Simulation Results

In this section, the results are presented in simulation, assuming that the voltage stack V_{st} corresponds to,

$$V_{st} = nV_c, \tag{3.37}$$

where $n \in \mathbb{R}_+$ is the number of cells in the stack, $V_c(\theta, \xi)$ is the voltage per cell presented in (3.11), and V_{st} is the stack voltage show in Fig. 3.1 *vs* FC current, and Fig. 3.2 corresponds to the voltage stack *vs* time. Likewise, the FC current *vs* time is presented in Fig. 3.3 where $\xi : \mathbb{R}_+ \to \mathbb{R}_+$ is formulated by

$$\xi = i_d A_{fc}, \tag{3.38}$$

where $i_d \in \mathbb{R}_+$ is the current density, $A_{fc} \in \mathbb{R}_+$ is the active surface in one cell.

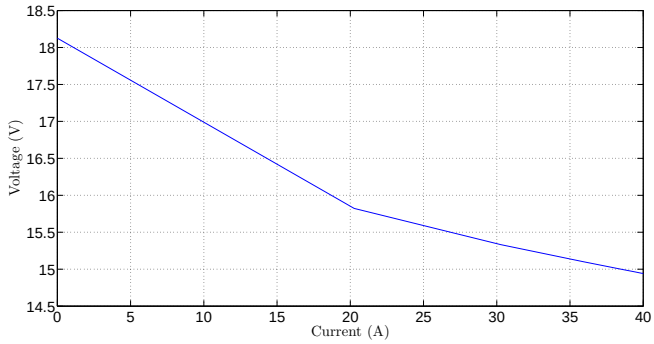

Figure 3.1: Polarization Curve PEM Fuel Cell BZ-100

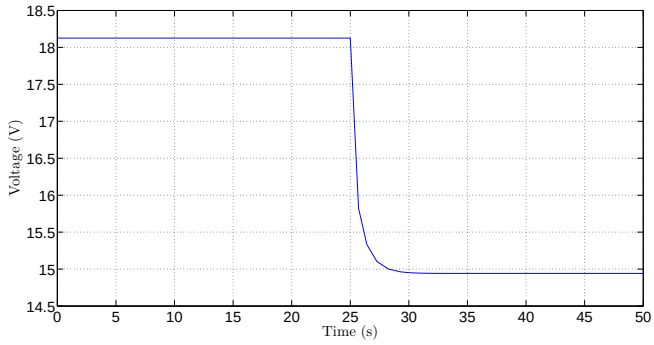

Figure 3.2: PEM Fuel Cell Stack Voltage (V_{st})

In Fig. 3.1, the voltage–current behavior in a PEMFC model BZ-100 is shown. In a 0 A, the curve starts at 18.1 V with a constant slope just to 20 A. When the pressure has changed, the slope becomes soft and the voltage decreases in small steps.

The voltage *vs* time curve of PEMFC describes a constant value of 18.1 V until 25 s in Fig. 3.2. After this time, it decreases to 15 V when the pressure is changing. In the case of the current, it has the same inverse behavior of 0 A until 25 s and after this time, the current reaches 40 A when the pressure has changed, see Fig. 3.3.

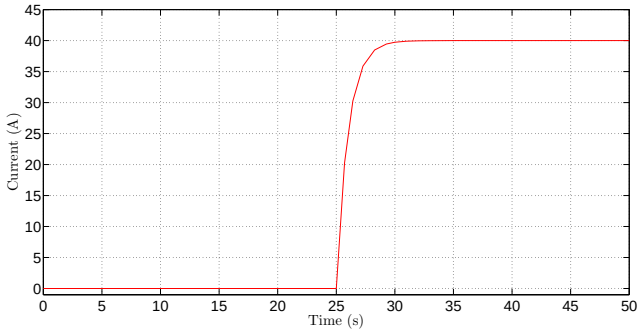

Figure 3.3: PEM Fuel Cell Stack Current (ξ)

The convergent estimator $\hat{\theta}$ is shown in different colors vs real values of pressure θ in a continuous blue line, which demonstrated is in Fig. 3.4 using seven different values for γ. In Fig. 3.5, we plot the increasing monotonic behavior to the partial differential term ϕ vs FC current and real value of oxygen pressure.

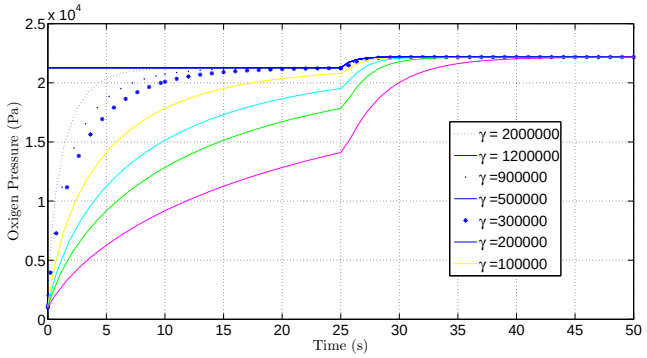

Figure 3.4: Real signal θ, Estimator $\hat{\theta}$ vs $time$

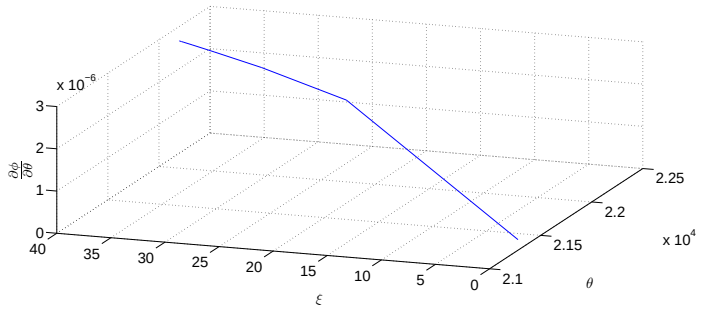

Figure 3.5: Monotonically increasing curve

We plan to prove these results, in the near future for an experimental plant to conclusively show the good performance of our globally convergent estimator of oxygen pressure.

3.6 Conclusions

This chapter has been showing that, with a suitable parameterization of the system that exhibits a monotonic behavior, it is possible to design a simple globally convergent (oxygen pressure) estimator for the PEMFC system using the principles of immersion and invariance theory recently reported in a control literature. Where a critical assumption is the compressor speed measurement, which in some practical applications might not be available. As clearly shown in section 3.3, the dependence of the voltage-current characteristic with respect to time is highly nonlinear, which renders its estimation a daunting task. Moreover, with the available measurements of temperature, flow, humidity, voltage, and current it seems difficult, if possible, to estimate an unknown variable (oxygen pressure). Two other challenging problems that are being currently investigated relate to the control of the PEMFC. There are some features that complicate this problem, stability is one that we can prove in a global form through the monotonicity conditions and the second, is the algebraic constraint. Experimental results will be implemented to prove the good performance of the oxygen pressure estimator in a real physical plant on a PEMFC BZ 100 test bench, however, here are only present the simulation curves that give us one tendency of convergence of our estimator.

Chapter 4

Conclusion and Future Work

Contents

4.1 Concluding remarks

This thesis contributes to an analytical solution for the dynamic energy transfer problem of interconnection systems. Specifically, we dealt with the problem for a system with some ports called "multiports" denoted by Σ_j. The proposed solution was to implement a DS–DER to generate the current or voltage references, to regulate the direction and rate of change of the power flow without relying on steady-state considerations; changing only the energy management policy $\alpha(t)$.

The DS–DER was presented and developed using standard switched power electronic devices in two ports assuming that the energy is conserved in a lossless system, that is to say, power–preserving nature of the DS–DER.

The simulation and experimental results with three different controls PI, FL, and input–output linearization were to prove the limitation of the DS–DER reported in Chapter 1. Chapters emphasi the behavior after a long–time when the energy transfer is not conserved because of losses in electrical elements of multiports and power electronic devices providing that the energy decreases asymptotically in the presence of dissipation, rendering the DS–DER asymptotically dysfunctional. Two ad–hoc modifications to overcome this fundamental shortcoming were proposed and tested in an experimental test

bench: (i) adding an outer–loop PI regulator for the DC–link voltage; and (ii) providing energy to the DER with an external source. The first alternative turned out to be inadequate, both from energy management and voltage regulation perspectives. On the other hand, adding an external battery effectively removed the problem, but does not seem to be a practically reasonable solution. It is important to overscore that the energy of the interconnection system always decreases in the DS–DER, hence its malfunction is still present even if we treat the battery as a third port—as done in the new DER.

Instead, it was proposed to drop the power–preserving feature of the DS–DER and new DER that takes into account the losses, was proposed. The new DER was tested in simulations and experiments using a simple PI scheme and an (approximate) input–output linearizing controller. The performance in both cases was excellent with the latter controller achieving, at the prize of higher complexity, a better regulation of the DC–link voltage. In addition to the new DER, an (ad–hoc) outer–loop switched PI controller, called a directional DER, was proposed and tested in simulations and experiments revealing excellent performance and ease of tuning.

The application of these ideas are currently being investigated for a realistic fuel–cell based system. Toward this end, novel multiport converter topologies are being explored to solve the same problems.

On the theoretical side, a question that remains to be addressed regards the robustness of the new DER, in particular, *vis–à–vis* parameter uncertainty. As shown in the experiments in subsection 2.2.3, the actual dissipation—whose value is needed to define the references—may differ significantly from the one predicted by the lumped parameter model. Hence, to enhance its robustness, an adaptive version of the DER must be worked out. Another interesting, though hard, theoretical question is the stability analysis of the directional DER. Invoking time–scale separation arguments this analysis seems feasible. However, this is not the scenario that was observed in our experimentation where, to obtain good performance, both loops must operate at the same time scale.

This work also provided the design for a simple globally convergent (oxygen pressure) estimator for a PEMFC system using the Immersion and Invariance Technique with a suitable system parameterization that exhibits a monotonic behavior. The oxygen pressure estimator is constructed considering a critical assumption for the flow measurement, that in some practical applications might not be available.

As clearly shown in section 3.3, the dependence of the voltage–current characteristic with respect to time is highly nonlinear, which renders its estimation a daunting task. Moreover, with the available measurements of temperature, flow, humidity, voltage, and current it seems difficult, if at all possible to estimate an unknown variable (oxygen pressure). Two other challenging problems that are currently being investigated relate to the control of the PEMFC. There are some features that complicate this problem, stability is one that we are proving in a global form through the monotonicity conditions

and the second the algebraic constraint.

4.2 Future work

The future tasks are to target to many directions because this particular strategy proposed solves general cases in domain of energy. Now, many applications could be realized with this idea not only in transport systems like electrical, hybrid, or fuel–cell vehicles. The potential applications of the new DER or the directional DER are beyond dc-to-dc converter configurations. Alternative topologies are available for handling ac-to-dc or ac-to-ac converters.

The mathematical analysis of stability on the modification of DS–DER will be considered for formulation, because the good results of this smart engineering idea that we have shown in this work are interesting.

Concerning the fuel cell and interconnection system set the opened the follow work to try both dynamics with adaptive multivariable control. Robustness should be tested without losing the stability properties in both systems. Also new controllers should be implemented in these strategies to know the performance of each one, before optimization.

The energy–loss estimation is also a problem to monitor during development and try these in microgrids, because as was shown in Chapter 2, doing the measurements for the losses demonstrate that there is no guaranty that we can compensate for all the dissipated energy due to the degradation of the components, variation of frequency and the even more uncertain losses involved in switching converters.

With regards to the subject of the fuel cell, the globally convergent estimator of pressure proposed here, has given us an excellent tendency of this variable, which should be implemented in an experimental manner.

Likewise, the next steps of this work are focused on to designing the observers in the dynamical model of fuel cell, using the same principles of I&I, reported recently in control theory, guaranteeing stability.

The next work will need to solve the estimation problem as it applies to variables of fuel cell such as temperature, humidity, current, etc, taking another condition even if the monotonicity tendency is increasing or not, exists for these particular mathematical relationships.

List of Figures

Appendix A

Appendix

A.1 Parameters of the power electronic implementation

Component	Value
L_1, L_2, L_3	195,193,210 μH
R_1, R_2, R_3	0.05 Ω
C_1, C_2	58 F
C_C	1.05 mF
R_C	1 $M\Omega$
V_b	10 V
Switching frequency	20 kHz

A.2 Mosfet Data-sheet implemented in the DER experiments

MITSUBISHI <MOSFET MODULE>

FM600TU-3A

HIGH POWER SWITCHING USE
INSULATED PACKAGE

FM600TU-3A

- $I_{D(rms)}$ 300A
- V_{DSS}.....150V
- Insulated Type
- 6-elements in a pack
- Thermistor inside
- UL Recognized
  Yellow Card No.E80276
  File No.E80271

APPLICATION

AC motor control of forklift (battery power source), UPS

OUTLINE DRAWING & CIRCUIT DIAGRAM Dimensions in mm

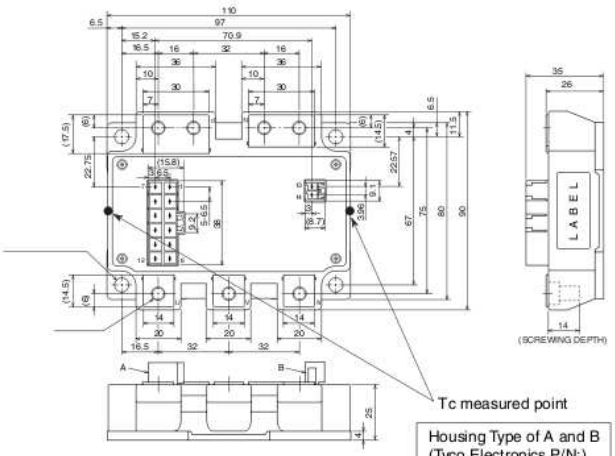

Housing Type of A and B
(Tyco Electronics P/N:)
A: 917353-1
B: 179838-1

CIRCUIT DIAGRAM

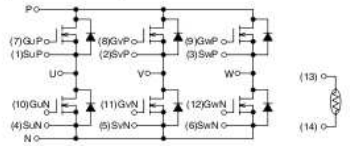

(1)SuP	(2)SvP	(3)SwP	(4)SuN	(5)SvN	(6)SwN	A
(7)GuP	(8)GvP	(9)GwP	(10)GuN	(11)GvN	(12)GwN	
(13)TH1	(14)TH2					B

May 2006

MITSUBISHI ELECTRIC

MITSUBISHI <MOSFET MODULE>

FM600TU-3A

HIGH POWER SWITCHING USE
INSULATED PACKAGE

ABSOLUTE MAXIMUM RATINGS (T_{ch} = 25°C unless otherwise specified.)

Symbol	Item	Conditions	Ratings	Unit
V_{DSS}	Drain-source voltage	G-S Short	150	V
V_{GSS}	Gate-source voltage	D-S Short	±20	V
I_D	Drain current	T_C' = 114°C*3	300	A
I_{DM}		Pulse*2	600	A
I_{DA}	Avalanche current	L = 10µH Pulse*2	300	A
I_S*1	Source current		300	A
I_{SM}*1		Pulse*2	600	A
P_D*4	Maximum power dissipation	T_C = 25°C	960	W
P_D*4		T_C' = 25°C*3	1300	W
T_{ch}	Channel temperature		−40 ~ +150	°C
T_{stg}	Storage temperature		−40 ~ +125	°C
V_{iso}	Isolation voltage	Main terminal to base plate, AC 1 min.	2500	V
—	Mounting torque	Main Terminal M6	3.5 ~ 4.5	N • m
		Mounting M6	3.5 ~ 4.5	N • m
—	Weight	Typical value	600	g

ELECTRICAL CHARACTERISTICS (T_{ch} = 25°C unless otherwise specified.)

Symbol	Item	Conditions		Limits Min.	Limits Typ.	Limits Max.	Unit
I_{DSS}	Drain cutoff current	V_{DS} = V_{DSS}, V_{GS} = 0V		—	—	1	mA
$V_{GS(th)}$	Gate-source threshold voltage	I_D = 30mA, V_{DS} = 10V		4.7	6	7.3	V
I_{GSS}	Gate leakage current	V_{GS} = V_{GSS}, V_{DS} = 0V		—	—	1.5	µA
$r_{DS(ON)}$ (chip)	Static drain-source On-state resistance	I_D = 300A, V_{GS} = 15V	T_{ch} = 25°C	—	1.6	2.2	mΩ
			T_{ch} = 125°C	—	3.0	—	
$V_{DS(ON)}$ (chip)	Static drain-source On-state voltage	I_D = 300A, V_{GS} = 15V	T_{ch} = 25°C	—	0.48	0.66	V
			T_{ch} = 125°C	—	0.91	—	
$R_{(lead)}$	Lead resistance	I_D = 300A terminal-chip	T_{ch} = 25°C	—	0.7	—	mΩ
			T_{ch} = 125°C	—	1.0	—	
C_{iss}	Input capacitance	V_{DS} = 10V, V_{GS} = 0V		—	—	110	nF
C_{oss}	Output capacitance			—	—	15	
C_{rss}	Reverse transfer capacitance			—	—	10	
Q_G	Total gate charge	V_{DD} = 80V, I_D = 300A, V_{GS} = 15V		—	1950	—	nC
$t_{d(on)}$	Turn-on delay time	V_{DD} = 80V, I_D = 300A, V_{GS1} = V_{GS2} = 15V, R_G = 4.2Ω, Inductive load switching operation, I_S = 300A		—	—	400	ns
t_r	Turn-on rise time			—	—	400	
$t_{d(off)}$	Turn-off delay time			—	—	500	
t_f	Turn-off fall time			—	—	400	
t_{rr}*1	Reverse recovery time			—	—	200	ns
Q_{rr}*1	Reverse recovery charge			—	8.0	—	µC
V_{SD}*1	Source-drain voltage	I_S = 300A, V_{GS} = 0V		—	—	1.3	V
$R_{th(ch-c)}$	Thermal resistance	MOSFET part (1/6 module)*7		—	—	0.13	°C/W
$R_{th(ch-c')}$		MOSFET part (1/6 module)*3		—	—	0.096	
$R_{th(c-f)}$	Contact thermal resistance	Case to fin, Thermal grease Applied*8 (1/6 module)		—	0.1	—	
$R_{th(c'-f')}$		Case to fin, Thermal grease Applied*3, *8 (1/6 module)		—	0.09	—	

THERMISTOR PART

Symbol	Parameter	Conditions	Limits Min.	Limits Typ.	Limits Max.	Unit
R_{TH}*6	Resistance	T_{TH} = 25°C*5	—	100	—	kΩ
B*6	B Constant	Resistance at T_{TH} = 25°C, 50°C*5	—	4000	—	K

*1: It is characteristics of the anti-parallel, source to drain free-wheel diode (FWDi).
*2: Pulse width and repetition rate should be such that the device channel temperature (T_{ch}) does not exceed T_{ch} max rating.
*3: T_C' measured point is just under the chips. If use this value, $R_{th(f-a)}$ should be measured just under the chips.
*4: Pulse width and repetition rate should be such as to cause negligible temperature rise.
*5: T_{TH} is thermistor temperature.
*6: $B = (\ln R_1 - \ln R_2)/(1/T_1 - 1/T_2)$ R_1: Resistance at T_1(K), R_2: Resistance at T_2(K)
*7: T_C measured point is shown in page OUTLINE DRAWING.
*8: Typical value is measured by using Shin-Etsu Chemical Co., Ltd "G-746".

May 2006

MITSUBISHI ELECTRIC

MITSUBISHI <MOSFET MODULE>

FM600TU-3A

HIGH POWER SWITCHING USE
INSULATED PACKAGE

PERFORMANCE CURVES

OUTPUT CHARACTERISTICS (TYPICAL) Chip

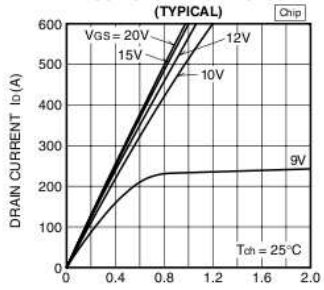

TRANSFER CHARACTERISTICS (TYPICAL) Chip

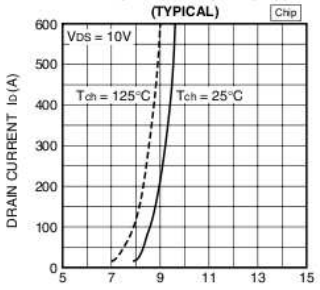

DRAIN-SOURCE ON-STATE VOLTAGE VS. TEMPERATURE (TYPICAL) Chip

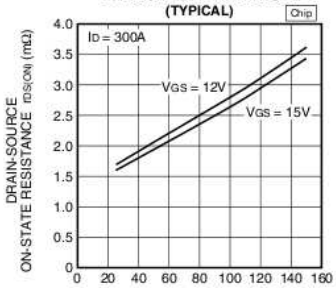

GATE THRESHOLD VOLTAGE VS. TEMPERATURE (TYPICAL)

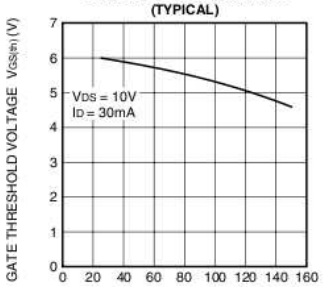

DRAIN-SOURCE ON-STATE VOLTAGE VS. GATE BIAS (TYPICAL) Chip

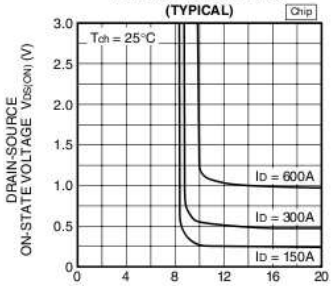

CAPACITANCE VS. DRAIN-SOURCE VOLTAGE (TYPICAL)

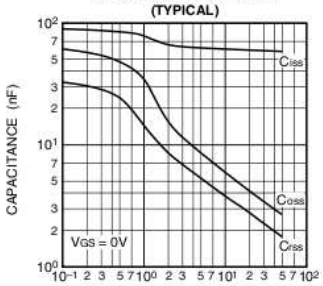

May 2006

MITSUBISHI ELECTRIC

MITSUBISHI <MOSFET MODULE>

FM600TU-3A

HIGH POWER SWITCHING USE
INSULATED PACKAGE

GATE CHARGE CHARACTERISTICS (TYPICAL)

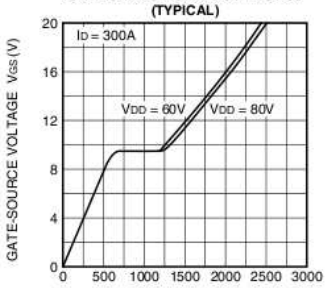

FREE-WHEEL DIODE FORWARD CHARACTERISTICS (TYPICAL)

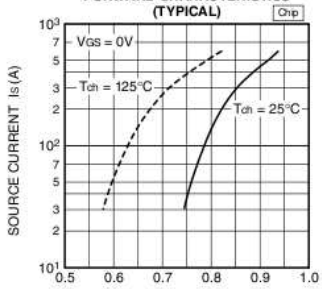

HALF-BRIDGE SWITCHING CHARACTERISTICS (TYPICAL)

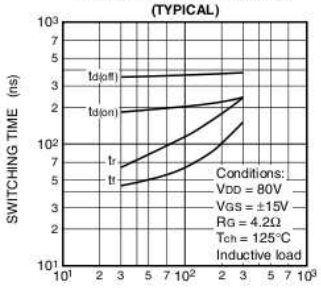

HALF-BRIDGE SWITCHING CHARACTERISTICS (TYPICAL)

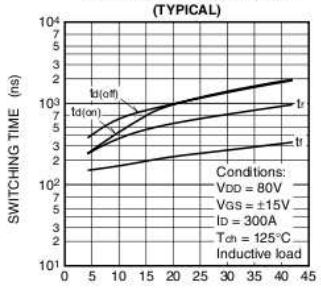

HALF-BRIDGE SWITCHING CHARACTERISTICS (TYPICAL)

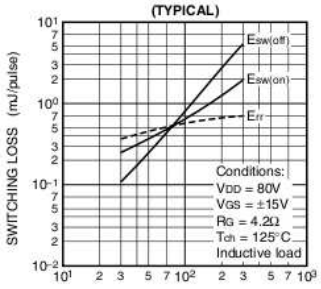

HALF-BRIDGE SWITCHING CHARACTERISTICS (TYPICAL)

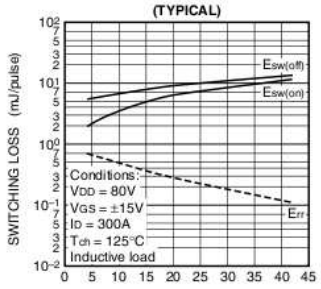

May 2006

MITSUBISHI ELECTRIC

FM600TU-3A

HIGH POWER SWITCHING USE
INSULATED PACKAGE

REVERSE RECOVERY CHARACTERISTICS
OF FREE-WHEEL DIODE
(TYPICAL)

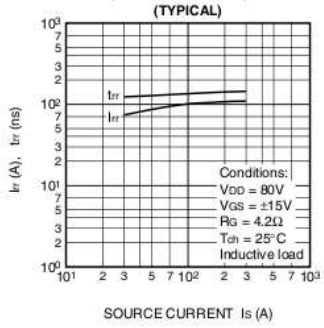

TRANSIENT THERMAL
IMPEDANCE CHARACTERISTICS

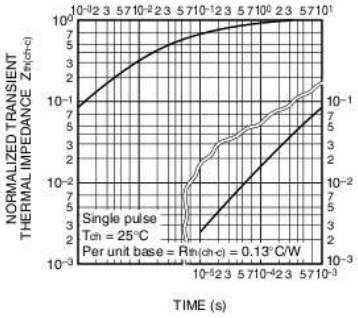

CHIP LAYOUT

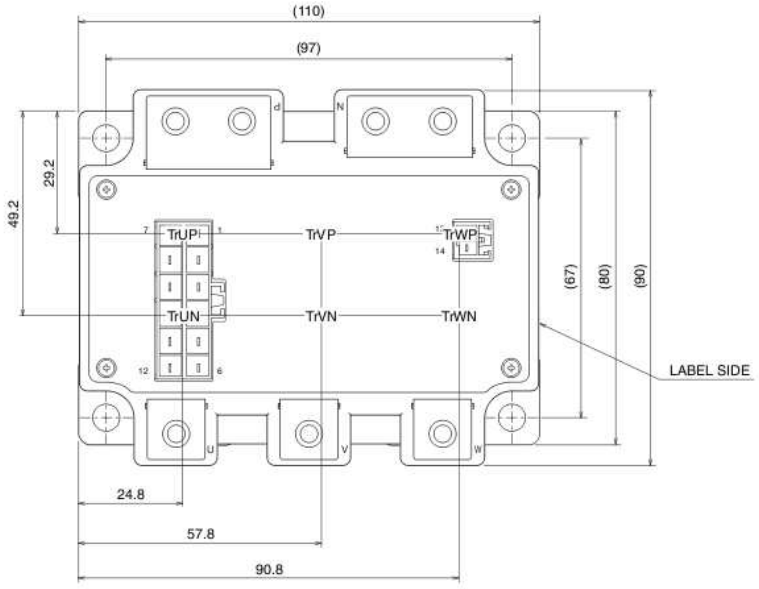

MITSUBISHI ELECTRIC

Appendix B

Appendix

B.1 PI controller constants

Controller	kp	ki
Current i_1	0.202	0.001
Current i_2	0.202	0.001
Current i_3	0.251	0.001
Voltage v_C	1.1084	0.357

Appendix C

Appendix

C.1 Constant values of PEMFC parameters

Symbol	Value
c_1	0.5
c_2	3.6642×10^{-1}
c_3	2036.5
c_4	10
c_5	2×10^{6}
c_6	0.78963×10^{-5}
c_7	0.83051×10^{-5}
c_8	8.52514×10^{-5}
c_9	0.47390
c_{10}	0.85791
c_{11}	0.368
c_{12}	7.08028×10^{-5}
c_{13}	18211
c_{14}	8.525
c_{15}	1×10^{-5}

C.2 Mathematical relationships of the variables

Symbol	Value
d_1	$1.229 - 8.5 \times 10^{-4}\, T_{st} + 8.5 \times 10^{-4}\, T_{atm}$
d_2	$4.30850 \times 10^{5}\, T_{st}$
d_3	$0.279 - 8.5 \times 10^{-4}\, T_{st} + 8.5 \times 10^{-4}\, T_{atm}$
d_4	$\frac{-1.61\times10^{-5} T_{st} + 1.618\times10^{-2}}{(1\times10^{5})^{2}}$
d_5	$1.8 \times 10^{-4} T_{st} - 1.6 \times 10^{-1}$
d_6	$-5.8 \times 10^{-4} T_{st} + 5.736 \times 10^{-1}$
A_1	$7.16 \times 10^{-4}\, T_{st} - 6.22 \times 10^{-1}$
A_2	$8.66 \times 10^{-5}\, T_{st} - 6.8 \times 10^{-2}$
B_1	$-1.45 \times 10^{-3}\, T_{st} + 1.68$
B_2	$-1.6 \times 10^{-4}\, T_{st} + 0.54$
C_3	2
$\lambda(\theta)$	$(\theta - 0.2346\, p_{atm} + 0.1173\, p_{sat})$

C.3 PEMFC commercial model BZ 100 constants

Symbol	Parameter	Value	Unit
T_{atm}	Atmospheric Temperature	298.15	K
p_{atm}	Atmospheric Pressure	101.32×10^{3}	Pa
ρ_{h_2}	Hydrogen Pressure	79.033×10^{3}	Pa
p_{sat}	Saturation Pressure Vapor	47.39×10^{3}	Pa
T_{st}	Fuel Cell Stack Temperature	313.15	K
A_{fc}	Cell Active Area	100	cm^2
I_{max}	Maxim Current density	2	A/cm^2

PEM-
fuel-cell-stacks

UBzM
ULMER BRENNSTOFFZELLEN MANUFAKTUR

PEM-fuel-cell-stack BZ 100

The PEM-fuel-cell-stack BZ 100 has an active area of 100 cm^2 per single-cell. The stack is provided with fuel gas (reformate or H_2) and oxidant (air or O_2) through external connectors and the gases are distributed to the single cells by internal manifolding. An additional cooling water circuit allows heat removal and the utilisation of the waste heat. The BZ 100 is working between a temperature range of 20°C up to 70°C and allows a pressurised operation up to 2 bar_{abs} on demand.

PEM-fuel-cell-stack BZ 100

Available configurations

Nominal load P [W]	Voltage U [V] @ nominal load	Dimensions (L x W x H) [mm]	Weight [kg]
100	2.4	130 x 140 x 140	4.5
250	6.0	180 x 140 x 140	5.9
500	12.0	250 x 140 x 140	8.5
1000	24.0	390 x 140 x 140	13.6

Caracteristic curve BZ 100

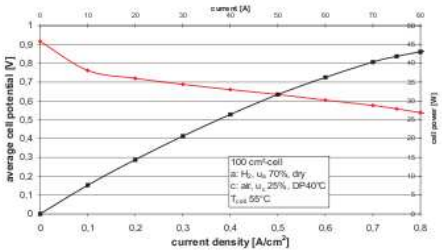

Caracteristic curve BZ 130

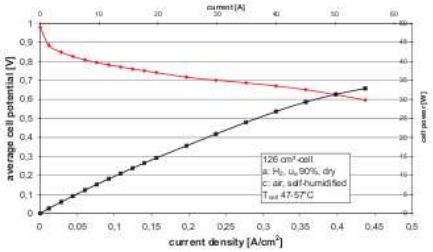

PEMFC-Stack BZ 130

The fuel-cell-stack BZ 130 has an external cathode gas manifolding open to the ambient air. For this reason the active area compared with the BZ 100 increases up to 126 cm^2. In addition to that you can use a radial fan for supplying that stack with air. The very low pressure drop between cathode-inlet and -outled makes by reducing peripheric losses a system very efficient. With a very simple air-recirculation-system, you can create a system-integrated air-humidifiacation. The BZ 130-stack is also with an air-cooled design available.

Available configurations

Nominal load P [W]	Voltage U [V] @ nominal load	Dimensions (L x W x H) [mm]	Weight [kg]
100	2.4	140 x 140 x 140	4.6
250	6.0	200 x 140 x 140	6.4
500	12.0	330 x 140 x 140	9.8
1000	24.0	580 x 140 x 140	16.4

PEM-fuel-cell-stack BZ 130

Dipl.-Ing. (FH) Klaus Steinhart
Phone: +49 (0) 731/9530-831, Fax: -888
Email: klaus.steinhart@ubzm.de

UBzM

Ulmer Brennstoffzellen Manufaktur GmbH
Helmholtzstr. 8, D-89081 Ulm
www.ubzm.de

Bibliography

[1] Jeffrey S. Gaffney, Nency A. Marley, "The impacts of combustion emissions on air quality and climate–from coal to biofuels and beyond," *Atmospheric Environment*, vol. 43, pp. 23-36, 2009.

[2] Christian Berggren, Thomas Magnusson, "Reducing automotive emissions–the potentials of combustion engine technologies and the power of policy," *Energy Policy*, vol. 41, pp. 636-643, 2012.

[3] Karl Georg Hoyer, "The history of alternative fuels in transportation: The case of electric and hybrid cars," *Utilities Policy*, vol. 16, pp. 63-71, 2008.

[4] J.M. Andujar, F. Segura, "Fuel cells: History and updating. A walk along two centuries," *Renewable and Sustainable Energy Reviews*, vol. 13, pp. 2309-2322, 2009.

[5] V. Ramirez, R. Ortega, R. Griñó, A. Sanchez-Squella and O. Bethoux, "Theory and experimental results of two dynamic energy routers," *2012 American Control Conference (ACC)*, June 27 - 29, 2012, Montreal, Canada.

[6] V. Ramirez, R. Ortega, A. Sanchez-Squella, O. Bethoux, R. Griñó, "Nouveau routeur dynamique prenant en compte les pertes : Theorie et résultats expérimentaux," *2012 7éme Conférence Internationale Francophone d'Automatique (CIFA)*, July 15 - 18, 2012, Grenoble, France.

[7] V. Ramirez, R. Ortega, O. Bethoux and A. Sanchez-Squella, "A dynamic router for microgrid applications: theory and experimental results," *Control Engineering Practice Journal*, vol. 27, pp. 23-31, 2014.

[8] Alessandro Astolfi, Dimitrios Karagiannis and Romeo Ortega, Nonlinear and Adaptive Control with Applications, Springer.

[9] Yoan D. Landau, Adaptive Control, Control and Systems Theory volume 8, Dekker, 1979.

[10] M. Chami, M. Ayad, A. Djerdir, and A. Miraoui, "Control study of fuel cell and supercapacitors system using hybrid dynamic nets,"in Proceedings of Industrial Electronics, 2008. *IEEE International Symposium on (ISIE 2008)*,(Cambridge, UK), pp. 1622-1626, July 2008.

[11] M.Y. Ayad, M. Becherif, A. Henni, A. Boubou, M. Wack, S. Laghrouche, "Passivity-Based Control applied to DC hybrid power source using fuel cell and supercapacitors," *Energy Conversion and Management*, vol. 51, pp. 1468-1475, 2010.

[12] M. Hilairet, M. Ghanes, O. Bethoux, V. Tanasa, J-P. Barbot, D. Normand-Cyrot, "A passivity-based controller for coordination of converters in a fuel cell system," *Control Engineering Practice*, vol. 21, pp. 1097-1109, 2013.

[13] V. Duindam and S. Stramigioli, "Port-based asymptotic curve tracking for mechanical systems," *European Journal of Control*, vol. 10, no. 5, pp. 411-420, 2004.

[14] Geoplex-Consortium, Modeling and Control of Complex Physical Systems: The Port Hamiltonian Approach. Springer-Verlag, 2009.

[15] H. Sira-Ramires, R. Silva-Ortigoza, Control Design Techniques in Power Electronics Devices, Springer, 2006.

[16] L. Zubieta and R. Bonet, "Characterization of double-layer capacitors for power electronics applications," *IEEE Trans. Industry Application*, vol. 36, pp. 199-205, July 2000.

[17] D. Casadei, G. Grandi, and C. Rossi, "A supercapacitor-based power conditioning system for a power quality improvement and uninterruptible power supply,"in Proceedings of Industrial Electronics, *IEEE International Symposium on (ISIE 2002)*, (L'Aquila, Italy), pp. 1247-1252, July 2002.

[18] John G. Kassakian and Martin F. Schlecht and George C. Verghese, Principles of Power Electronics, Addison Wesley, 1991.

[19] S. Sanders and G. Verghese, "Lyapunov-based control for switched power converters," *IEEE Trans. Power Electronics*, vol. 7, No. 1, pp. 17-24, 1992.

[20] R. Ortega, A. Loria, P. J. Nicklasson and H. Sira-Ramirez, Passivity-Based Control of Euler-Lagrange Systems, Springer-Verlag, 1998.

[21] M. Hernandez-Gomez, R. Ortega, F. Lamnabhi-Lagarrigue and G. Escobar, "Adaptive PI Stabilization of Switched Power Converters," *IEEE Trans. Control Systems Technology*, vol. 18, No. 3, pp. 688-698, 2010.

[22] S. Malo and R. Griñó, "Design and construction of an electric energy conditioning system for a PEM type fuel cell," *Proceedings of the 33rd Annual Conference of the IEEE Industrial Electronics Society (IECON07)*, Taipei, Taiwan, pp. 1633-1638, November 2007.

[23] P. Thounthong, S. Raël and B. Davat, "Energy management of fuel cell, battery, supercapacitor hybrid power source for vehicle applications," *Journal of Power Sources*, vol 193, no. 1, pp. 376-385, August 2009.

[24] R. Erickson and D. Maksimovic, Fundamentals of Power Electronics, Kluwer Academic Publishers, 2004.

[25] K. Ogata, Modern Control Engineering, Prentice-Hall, 2003.

[26] H. Khalil, Nonlinear systems, 3rd ed., Prentice-Hall, Upper Saddle River, N.J, 2002.

[27] G. Joós and J. Espinoza, "Three-phase series var compensation based on a voltage-controlled current source inverter with supplemental modulation index control," *IEEE Trans. Power Electronics*, vol. 14, No. 3, pp. 587-598, May 1999.

[28] Benjamin C. Kuo, Automatic Control Systems, 7a ed., Prentice-Hall, 1996.

[29] A. Sanchez, Energy Management in Electric Systems Fed by Fuel Cell Stacks, Ph.D. Thesis, Université Paris-Sud XI, March 2011.

[30] W. Choi, J. W. Howze and P. Enjeti, "Fuel-cell powered uninterruptible power supply systems: Design considerations," *Journal of Power Sources*, vol 157, pp. 311-317, June 2006.

[31] M. E. Schenck, J. Lai and K. Stanton, "Fuel cell and power conditioning system interactions," *Proceedings of the 20th Annual IEEE Applied Power Electronics Conference and Exposition (APEC05)*, Austin, Texas, USA, pp. 114-120, March 2005.

[32] A. Sánchez-Squella, R. Ortega, R. Griñó and S. Malo, "Dynamic energy router," *IEEE Control Systems Magazine*, vol. 30, No. 6, pp. 72-80, 2010.

[33] H. Fraghani,"The path of the smart grid," *IEEE Power and Energy Magazine*, vol. 8, No. 1, pp. 18-28, 2010.

[34] R. Ortega, A. van der Schaft, F. Castaños and A. Astolfi,"Control by state-modulated interconnection of port-Hamiltonian systems," *IEEE Trans. Automat. Contr.*, vol. 53, No. 11, pp. 2527-2542, 2008.

[35] Miguel Carrasco, Fernando Mancilla-David and Romeo Ortega, "A globally convergent estimator of solar irradiance in photovoltaic panels," *Conference on Decision and control*, submit March 2013.

[36] Miguel Carrasco, Fernando Mancilla-David and Romeo Ortega, "An estimator of solar irradiance in photovoltaic arrays with guaranteed stability properties," *IEEE Trans. on Industrial Electronics*, vol. 61, No. 7, July 2014.

[37] Xiangbin Liu, Romeo Ortega, Hongye Su and Jian Chu, "On adaptive control of nonlinearly parameterized nonlinear systems," *Systems and Control Letters*, vol. 10, No. 1, pp. 36-43, January 2011.

[38] Xiangbin Liu, Romeo Ortega, Hongye Su and Jian Chu, "Immersion and invariance adaptive control of nonlinearly parameterized nonlinear systems," *IEEE Trans. Autom. Control*, vol. 55, No. 9, pp. 2209-2214, September 2010.

[39] Romeo Ortega, Fernando Mancilla-David and Fernando Jaramillo, "A Globally Convergent wind speed estimator for wind turbine systems," *International Journal of Adaptative control and Signal Processing*, March 2012.

[40] Alessandro Astolfi, Romeo Ortega, "Immersion and invariance: A new tool for stabilization and adaptive control of nonlinear systems," *IEEE Trans. Autom. Control*, vol. 48, No. 4, April 2003.

[41] S. Townley, "An example of a globally stabilizing adaptive controller with a generically destabilizing parameter estimate," *IEEE Trans. Autom. Control*, vol. 44, No. 4, pp. 2238-2241, November 1999.

[42] Reine Talj, Modélisation et Commandes non Linéaires du système d'air de Piles à Combustible Type PEM, Ph.D. Thesis, Université Paris-Sud XI, October 2009.

[43] Jay Tawee Pukrushpan, Modeling and Control of Fuel Cell Systems and Fuel Processors, Ph.D. Thesis, The University of Michigan, 2003.

[44] James Larminie and Andrew Dicks, Fuel Cell Systems Explained, Wiley, 2003.

[45] Frano Barbir, PEM Fuel Cells: Theory and Practice, Elsevier, 2005.